8-1-2012

Numerical and Experimental Investigation of the Stability Region for a Cylindrical Ion Trap

Bradley Steven Clarke
University of Nevada, Las Vegas, bradley.steven.clarke@gmail.com

NUMERICAL AND EXPERIMENTAL INVESTIGATION OF THE STABILITY REGION FOR A CYLINDRICAL ION TRAP

by

Bradley S. Clarke

Bachelor of Science in Physics
University of Nevada Las Vegas
2009

Bachelor of Science in Mathematics
University of Nevada Las Vegas
2009

A thesis submitted in partial fulfillment of
the requirements for the

Masters of Science in Physics

Department of Physics and Astronomy
College of Sciences
The Graduate College

University of Nevada, Las Vegas
August 2012

UNLV
UNIVERSITY OF NEVADA LAS VEGAS

THE GRADUATE COLLEGE

We recommend the thesis prepared under our supervision by

Bradley Clarke

entitled

Numerical and Experimental Investigation of the Stability Region for a Cylindrical Ion Trap

be accepted in partial fulfillment of the requirements for the degree of

Masters of Science in Physics
Department of Physics and Astronomy

Victor Kwong, Ph.D., Committee Chair

David Shelton, Ph.D., Committee Member

Stephen Lepp, Ph.D., Committee Member

Balakrishnan Naduvalath, Ph.D., Graduate College Representative

Thomas Piechota, Ph. D., Interim Vice President for Research and Graduate Studies and Dean of the Graduate College

August 2012

ABSTRACT

Numerical and Experimental Investigation of the Stability Region for a Cylindrical Ion Trap

By

Bradley S. Clarke

Dr. Victor Kwong, Examination Committee Chair
Professor of Physics
University of Nevada, Las Vegas

The stability diagram provides a useful tool for determining the appropriate AC biased potential to confine ions in an ion trap. Since no analytic solution exists for the cylindrical ion trap's (CIT's) equations of motion, the CIT's stability region is not well known. The objective of this thesis is to determine the stability region for a CIT numerically and experimentally. The equations of motion for ions confined in a CIT are derived and found to be similar to the Mathieu equation, i.e. the equation that describes ion motion in a hyperbolic ion trap (HIT). Because of the similarities in the equations of motion for the two traps, and since the stable region for a HIT is well known, the HIT is used as a guide for the determination of the CIT's stable region. The HIT stability region is determined by numerical calculations for comparisons with the analytic HIT stable region in order to test the validity of the numerical method. In this investigation, the ion kinetic energy is found to influence the shape of the CIT's stable region. The locations of the CIT's $\beta_z = 0$ and $\beta_r = 0$ stability boundaries, i.e. for unstable trajectories in the axial and radial directions respectively, are experimentally determined through measuring the number density of N^+ at multiple locations in the stability diagram. The experimentally determined boundaries for $\beta_z = 0$ and $\beta_r = 0$ are found to lie consistently between the 0.01eV and 0.1eV numerically calculated energy dependent boundaries for the CIT.

ACKNOWLEDGEMENTS

I would like to thank my advisor Dr. Victor Kwong for igniting my interest in the field of atomic, molecular, and optical physics as well as giving me the opportunity to do research in this field. I will never forget our numerous discussions on physics and life in general where your shared wisdom will be with me for the rest of my life.

I would also like to thank Bill O'Donnell for building numerous electronic circuits that helped to optimize the experimental facility. Thank you to the rest of my committee, Dr. Stephen Lepp, Dr. David Shelton, and Dr. Balakrishnan Naduvalath for listening and critiquing my long presentations and thesis paper.

To my friends and colleagues Athos Kyriakides, Jason Baker, Daniel Antonio, Martin Galley, John Howard, and Greg Collarch, you made my graduate experience much more enjoyable. I will never forget the numerous hours we spent working on assignments together, the long days spent in the laboratory, or the great times we shared after working hours. I hope that we will all remain in touch for years to come.

Finally, I would like to thank my family for their undying support through the good times and the bad. I would never have made it this far without their love and help. Thank you.

TABLE OF CONTENTS

LIST OF FIGURES

CHAPTER 1

INTRODUCTION

Commonly referred to as the Paul trap due to Wolfgang Paul's discovery of the two dimensional variant of the device in 1953 [1], the RF quadrupole ion trap has revolutionized the field of atomic, molecular, and optical physics. With its feasibility first demonstrated in the late 1950's by Berkling [2] and Fischer [3], the Paul trap localizes ions in space through the application of a biased AC potential to its hyperbolic ring electrode. This ion localization has allowed physicists to probe an ion's various properties, such as the lifetime of an ion's metastable state and charge transfer rates with neutral atoms/molecules to name a few [4].

One drawback in using a Paul trap in experimental research is its difficulty in construction due to the hyperbolic geometry of its electrodes. Another disadvantage of the Paul trap, when used in conjunction with a time of flight (TOF) mass spectrometer, is the difficulty posed in ejecting ions from the trap for subsequent analysis. Since the complex shape of the Paul trap requires its electrodes to be made from solid pieces of metal, ion extraction cannot be achieved unless modifications to its geometry are made. To circumvent such issues, alternate geometries can be utilized to confine ions for experimentation, notably an ion trap with cylindrical geometry.

Constructed with a cylindrically shaped ring electrode and two flat endcaps, the cylindrical ion trap (CIT) has been shown to approximate the potential surfaces of the Paul trap near the trap's center [5]. Also, the CIT is much easier to fabricate compared to the Paul trap [6]. By constructing the electrodes out of wire mesh, ions can be easily extracted from a CIT by the application of high voltages to its endcaps. An additional advantage of constructing the trap entirely out of wire mesh is that the gas pressure inside the ion trap is the same as the vacuum chamber pressure. Thus the gas density inside the ion trap can be monitored by ion gauges external to the trap.

Although the CIT has many advantages compared to the Paul trap, there is one major disadvantage in using a CIT, i.e. its complex mathematical description of the ion trajectories. Unlike the CIT, the equations of motion for ions confined by the Paul trap are of the form of the 2^{nd} order Mathieu differential equation [7]. The solutions to this equation are well known where stable ion motion exists for certain values of the Mathieu parameters [7]. The parameters that lead to stable ion motion can be represented in a "stability diagram," where the boundaries between stable and unstable regions are well defined. With the Mathieu parameters dependent upon the mass-to-charge ratio of an ion, the stability diagram can be exploited in such a way so as to expel unwanted ions from the trap while confining other ions of interest. This is a feature of considerable importance in mass spectrometry. In order to operate the CIT in a similar manner, its stability region must be determined.

This thesis focuses on the determination of the CIT stable region through numerical calculations and experimental measurements where it is organized in the following way. Chapter 2 includes a theoretical description of the Paul trap and CIT. Chapter 3 describes the method used to numerically determine the stable region of a CIT as well as how the ion energy influences the shape of the stable region. A numerical calculation of the stable region for a Paul trap is also included in this chapter to test the validity of the numerical method. Chapter 4 describes the apparatus utilized in the experiment as well as the procedure and methods used to determine the experimental boundaries from the measurements. In Chapter 5, the results of the measurements are presented where comparisons are made to the numerically determined boundaries of the CIT.

CHAPTER 2

THEORETICAL BACKGROUND

This chapter presents the theoretical framework necessary for describing the trajectories of ions confined by a cylindrical ion trap (CIT) and a Paul trap, referred to as the hyperbolic ion trap (HIT) throughout this thesis to emphasize the trap's geometry. The CIT equations of motion are derived and it will be shown that they are similar to the HIT equations of motion. Even though the current research focuses on the properties of the CIT, the essential features of the HIT are also included in the discussion to gain insight into the stability of trapped ions in a CIT.

Hyperbolic Ion Trap (HIT)

A HIT consists of hyperbolic electrodes with a biased AC potential applied to its ring electrode. With the application of this potential, charged particles can be localized within the trap where their position, momentum, and energy are governed by the generated dynamic electric field. A diagram of the HIT is included in Figure 1.

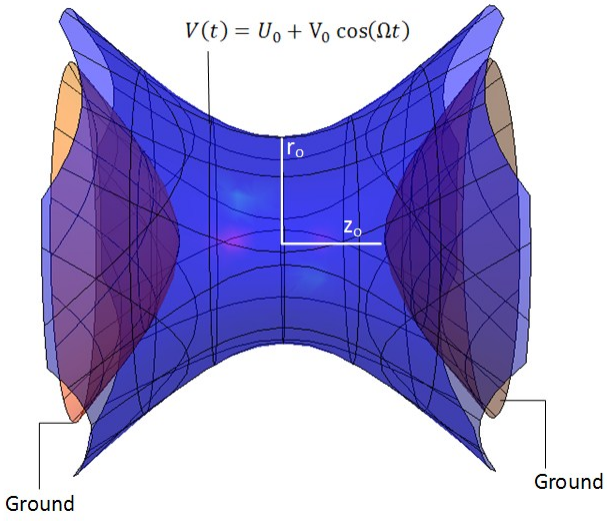

Figure 1: The hyperbolic ion trap (HIT).A time varying potential V(t) is applied to the ring electrode where U_0 is the DC offset, V_0 is the amplitude of the time varying part of the potential with angular frequency **Ω**. The endcaps are held at ground.

Since its invention, numerous investigations on the properties of the HIT have been performed. Since an extensive body of work exists for the HIT, notably the work performed by Dawson et al. [8-17] and Todd et al. [18-22], only the essential features of the HIT will be presented in this thesis. With the geometry and applied potential specified in Figure 1, an ion's equations of motion are of the form of the 2nd order Mathieu differential equation

$$\frac{d^2u}{dv^2} + \left(a_u - 2q_u\cos(2v)\right)u = 0, \tag{2.1}$$

where u represents the motion in the x, y, or z direction and $v = \frac{\Omega t}{2}$. The Mathieu parameters that appear in Eq. 2.1, a_u and q_u, are dependent upon the geometry of the trap r_o and z_o, the applied potential V_o and U_o, angular frequency Ω, the mass m and charge q of the confined ion as seen in the following equations:

$$q_z = -2q_r = \frac{q}{m}\frac{8\,V_0}{(r_0^2 + 2z_0^2)\Omega^2} \tag{2.2}$$

$$a_z = -2a_r = -\frac{q}{m}\frac{16\,U_0}{(r_0^2 + 2z_0^2)\Omega^2}, \tag{2.3}$$

where r represents the motion in either the x or y direction and are identical due to azimuthal symmetry [7]. The Mathieu equation is well known and previous work has shown that its solutions have the following form

$$u(v) = \alpha' e^{\mu v}\sum_{-\infty}^{\infty} C_{2n}\, e^{2inv} + \alpha'' e^{-\mu v}\sum_{-\infty}^{\infty} C_{2n}\, e^{-2inv}, \tag{2.4}$$

where α' and α'' are dependent upon the ion's initial position and velocity where the parameters μ and C_{2n} are dependent only upon the Mathieu parameters [23, 24].

There are two types of solutions to the Mathieu equation: stable and unstable, which are determined by the value of μ. Stable solutions require $\mu = i\beta_u$, where β_u is a real non-integer number [23, 24]. Integer values of β_u, i.e. Mathieu functions of integral order, form a series of

solutions that are aperiodic, hence unstable. These functions form the boundary between stable and unstable regions in a_u and q_u space and are used to generate what is called the "stability diagram." One important property of the HIT is that ion stability is independent of the ion's initial position and velocity. Noting that $a_z = -2a_r$ and $q_z = -2q_r$, the stability diagram in a_z and q_z space for $0 \leq \beta_{r,z} \leq 3$ is shown in Figure 2. For successful ion confinement to occur, the ion must have a stable trajectory in both the axial and radial directions. The Mathieu parameters that lead to this type of confinement are indicated in Figure 2 by the overlap of the z-Stable and r-Stable shaded regions. In the current investigation, we focus on the $0 < \beta_{r,z} < 1$ boundaries. Accessing the higher order stable regions is possible but would require values for U_0 that are an order of magnitude or larger than that needed for the first stable region.

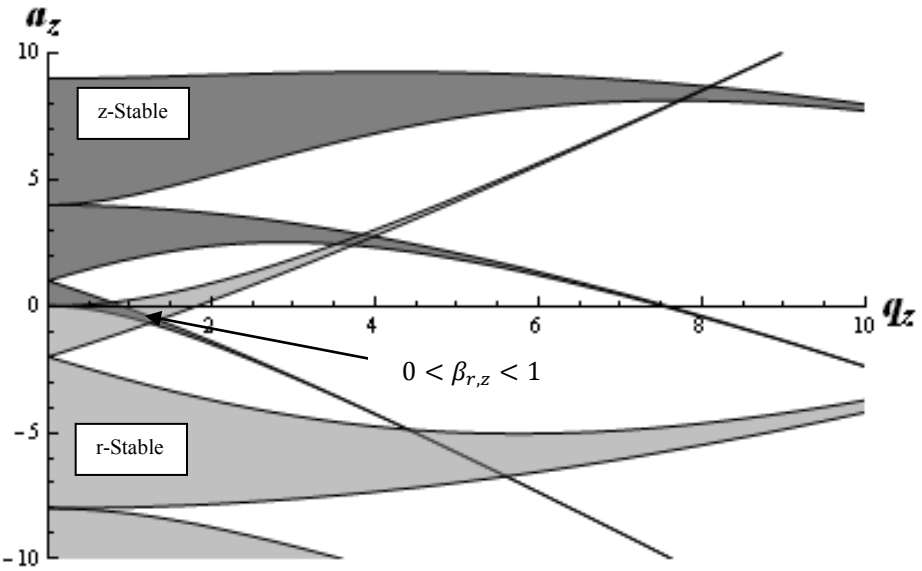

Figure 2: The HIT stability diagram for $0 \leq \beta_{r,z} \leq 3$. The dark shade represents regions where ions have stable axial trajectories where the lighter shade represents the regions where ions have stable radial trajectories. The arrow marks the location where the z-stable and r-stable overlap for $0 < \beta_{r,z} < 1$.

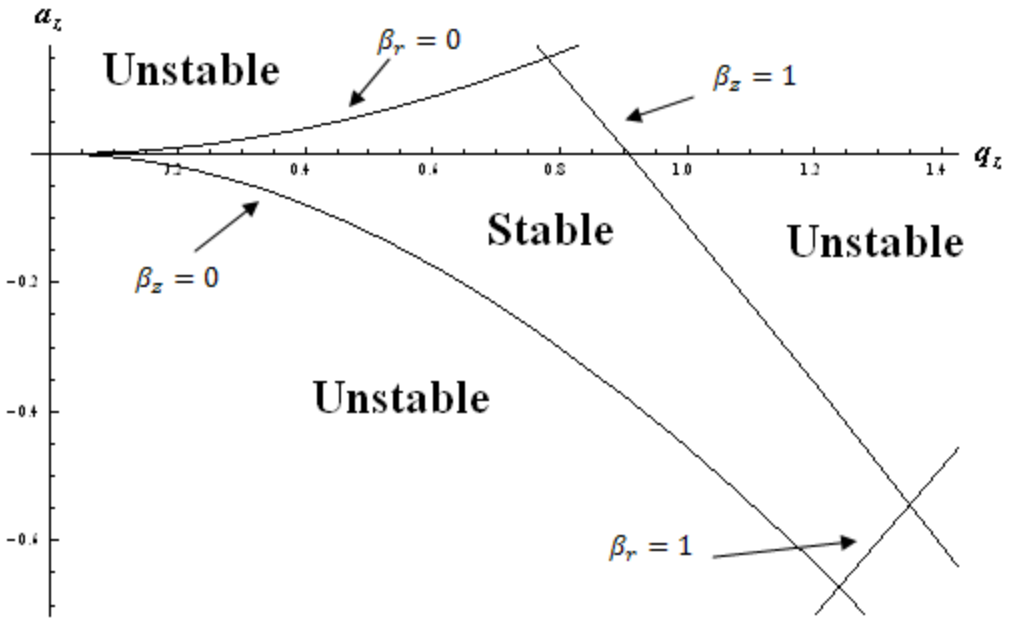

Figure 3: The HIT stability diagram for $0 \leq \beta_{r,z} \leq 1$. The region marked stable indicates the possible values for the Mathieu parameters that lead to stable ion trajectories inside a HIT. For values that lie outside this region, the ion will not have a stable ion trajectory and thus cannot be confined in the trap.

In Figure 3, the four Mathieu functions of integral order are denoted by the degree of freedom in which the ion trajectory is unstable, r or z, as well as the integral order of the function, 0 or 1. The Mathieu parameters that lie just beyond the $\beta_z = 0$ or 1 boundary lead to an aperiodic trajectory that is axially unstable. Likewise, parameters that lie just beyond the $\beta_r =$ 0 or 1 boundary are aperiodic and unstable in the radial direction. These unstable trajectories arise due to a value for μ that is not purely imaginary, leading to non periodic terms in the analytic solution to the Mathieu in Eq. 2.4 [24]. For ion trapping to be successful, the ion must have a stable trajectory in all degrees of freedom which can be achieved with Mathieu parameters located in the region marked stable in Figure 3.

Cylindrical Ion Trap (CIT)

In order to determine the similarities and differences between confining ions in a HIT and a CIT, the time dependent potential surface inside a CIT must be determined. Using the boundary conditions specified in Figure 4 and excluding the influence of space charge and collisions, the potential can be found by solving Laplace's equation:

$$\begin{cases} \nabla^2\phi(r,z) = 0 \\ \phi(r_0,z) = V(t) \\ \phi(r,z_0) = 0 \end{cases} \tag{2.5}$$

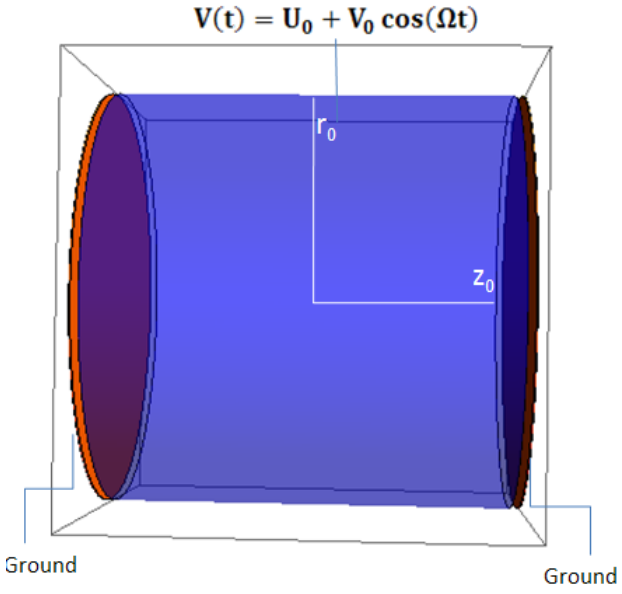

Figure 4: The cylindrical ion trap (CIT). A time varying potential V(t) is applied to the ring electrode where U_0 is the DC offset, V_0 is the amplitude of the time varying part of the potential with angular frequency Ω. The endcaps are held at ground.

Noting the symmetry in the azimuthal direction, separation of variables can be used

$$\phi(r,z) = \mathcal{R}(\ell r)\mathcal{Z}(z) \tag{2.6}$$

where ℓ is a constant to be determined. Using the Laplacian in cylindrical coordinates, and after some algebra, the equations describing the potential in the two coordinate directions are

$$\begin{cases} r^2\mathcal{R}'' + r\,\mathcal{R}' - r^2\mathcal{R} = 0 \\ \mathcal{Z}'' = -\ell^2\mathcal{Z} \end{cases} \tag{2.7}$$

where the primes represent the total derivative with respect to the independent variables r and z for the functions $\mathcal{R}$ and $\mathcal{Z}$ respectively.

The form of the radial equation is known as the Modified Bessel differential equation of order zero which has the following solution

$$\mathcal{R}(\ell r) = A\,I_0(\ell r) + B\,K_0(\ell r). \tag{2.8}$$

The functions I_0 and K_0 represent the zeroth order Modified Bessel functions of the first and second kind respectively where A and B are coefficients dependent upon the boundary conditions. Note that for the potential to be finite at the origin, the coefficient B must be zero since $\lim_{r\to 0} K_n$ tends to infinity.

The solution for the potential in the axial direction has the form

$$\mathcal{Z}(z) = C\sin(\ell z) + D\cos(\ell z) \tag{2.9}$$

When using the boundary conditions specified in Eq. 2.5, one may be tempted in setting D to zero to find the solution for the potential; however, the sine function is not symmetric about the origin. Therefore, by setting C to zero one finds that

$$\ell_n = \frac{2n+1}{z_0}\frac{\pi}{2}. \tag{2.10}$$

Using the remaining boundary condition in Eq. 2.5 and summing over all possible solutions, the potential inside the CIT is

$$\phi(r,z,t) = 4V(t)\sum_n \frac{\cos(n\pi)}{(2n+1)\pi}\frac{I_0(\ell_n r)}{I_0(\ell_n r_0)}\cos(\ell_n z) \tag{2.11}$$

Through using the potential in Eq. 2.11, the equations of motion for ions inside the CIT can be derived. Starting with the Lorentz equation,

$$\vec{F} = q\vec{E} = -q\vec{\nabla}\Phi \tag{2.12}$$

where q represents the charge of the ion. Upon differentiating the potential, the equations of motion in the axial and radial directions for an ion of mass m have the following form:

$$m\ddot{z} = q\frac{2V(t)}{z_0}\sum_n \cos(n\pi)\frac{I_0(\ell_n r)}{I_0(\ell_n r_0)}\sin(\ell_n z) \tag{2.13}$$

$$m\ddot{r} = -q\frac{2V(t)}{z_0}\sum_n \cos(n\pi)\frac{I_1(\ell_n r)}{I_0(\ell_n r_0)}\cos(\ell_n z) \tag{2.14}$$

where the double dot represents the second total derivative with respect to time.

Assuming the dimensions of the CIT have the relation $r_0 = z_0$, the following functions are used to simplify the equations of motion:

$$\eta(r,z) = \frac{3z_0}{2z}\sum_n \cos(n\pi)\frac{I_0(\ell_n r)}{I_0(\ell_n r_0)}\sin(\ell_n z) \tag{2.15}$$

$$\chi(r,z) = \frac{3z_0}{r}\sum_n \cos(n\pi)\frac{I_1(\ell_n r)}{I_0(\ell_n r_0)}\cos(\ell_n z) \tag{2.16}$$

It may not seem obvious here, yet Eq. 2.13-14 are similar to the 2nd order Mathieu differential equation which describes the trajectories of ions in a HIT. Through using the Mathieu parameters defined in Eq. 2.2-3, the equations of motion for ions confined by a CIT have the following simplified form

$$\frac{d^2z}{dv^2} + \left(a_z - 2q_z\cos(2v)\right)z\,\eta(r,z) = 0 \tag{2.17}$$

$$\frac{d^2r}{dv^2} + \left(a_r - 2q_r\cos(2v)\right)r\,\chi(r,z) = 0 \tag{2.18}$$

where $v = \frac{\Omega t}{2}$.

Note that Eq. 2.17 and 18 are close to the form of the 2nd order Mathieu differential

equation, i.e. Eq. 2.1, where the difference lies with the inclusion of the functions $\eta(r, z)$ and $\chi(r, z)$ in the equations. The appearance of these terms couples the motion of the ion due to the dependence of both z and r in each function. Because of this, no analytic solution exists for Eq. 2.17 and 2.18. Therefore, the stability region for ions confined by a CIT must be determined through numerical calculations.

In the case of small displacements about the trap's center, the functions $\eta(r, z)$ and $\chi(r, z)$ are effectively constant (see Appendix I). In this special case, one can use the pseudopotential well model adopted by Knight for the HIT to describe ion motion inside the CIT [4]. Nevertheless, this description is limited to the region where $\eta q_z \leq 0.4$. A detailed description of the pseudopotential well model for the CIT is included in Appendix II.

CHAPTER 3

NUMERICAL CALCULATION OF THE STABLE REGION

As discussed in Chapter 2, the stability of ion trajectories confined by a HIT is dependent only upon the Mathieu parameters. For a CIT, ion motion is coupled between the axial and radial directions due to the appearance of Eq. 2.15 and 2.16 in Eq. 2.17 and 2.18 respectively. As a consequence, the stability of an ion's trajectory in a CIT is dependent upon the Mathieu parameters as well as the ion's initial position and velocity. This chapter discusses how the stability boundaries for the HIT and the CIT are numerically determined where the approach is similar to the one used by Lee et al. in their calculation of the stable region for a miniaturized CIT [25].

Numerical Calculation of the HIT Stable Region

Since no analytic solution exists for Eq. 2.17 and Eq. 2.18, the stable region boundaries for a CIT must be determined through numerical methods. To test the validity of this approach, the stability region for a HIT is also determined numerically and compared to the well established HIT stability region. The procedure for numerically determining the HIT boundary consists of the following steps:

1. With m/q=14 amu/e and $\nu = 600\text{KHz}$, Mathieu parameters are selected.
2. Initial position of ion set to 1nm displacement from trap's origin and zero initial kinetic energy in each degree of freedom.
3. Eq. 2.1 is numerically solved in Mathematica using the 4^{th} order Runge Kutta method.
4. If the calculated trajectory is
    a. Periodic (bounded motion): ion is considered stable and steps 1-3 are repeated with a different value for $\mathbf{a_z}$.

b. Aperiodic (unbounded motion): ion is considered unstable.

5. For fixed q_z, the a_z value of the boundary point is set as the average between the a_z values that lead to the aperiodic trajectory and the last periodic trajectory.

For the sake of consistency, the same frequency and mass-to-charge ratio used in the boundary mapping experiment, discussed in Chapter 4, are also used in step 1 in the above procedure. In step 2, a non-zero displacement from the trap's origin is used for the ion's initial position. The small displacement is needed due to the symmetry of the trap, where an ion situated at the exact center of the trap with no kinetic energy will theoretically remain trapped regardless of the values used for the Mathieu parameters. The 4th order Runge Kutta method approximates the analytical solutions to the Mathieu equation to a high degree of accuracy and is used in step 3 of the above procedure. A variable step size is used in the calculation and never exceeds 167 ns, or 1/10 of the period of the selected frequency. This maximum step size ensures that all features of the ion trajectory is calculated including the ion's response to the driving field, i.e. the micromotion for small values of q_z as discussed in Appendix II. To illustrate steps 4 and 5 for the $\beta_z = 0$ boundary, example trajectories for $q_z = 0.4636$ are shown in Figure 5.

When determining the a_z value of the boundary point, a step size of -0.0009 for a_z is used. The search starts with a_z inside the stable region and ends when the ion becomes unstable as viewed through a plot of the ion displacement as a function of time. Figure 5 shows the last two ion trajectories using this search scheme for $q_z = 0.4636$. As seen in Figure 5a, the axial ion trajectory is stable for the selected Mathieu parameters due to its periodic ion trajectory. In Figure 5b, the ion trajectory is unstable due to its aperiodic trajectory and escapes the physical boundaries of the ion trap in just under 400μs. The numerically determined a_z boundary point is taken as the average between these two steps, i.e. $a_z = -0.1052 \pm 5 \times 10^{-4}$, which is in agreement with the theoretical boundary value of -0.1051. This scheme is performed for 72 different locations in the stability diagram to map the boundary of the stable region.

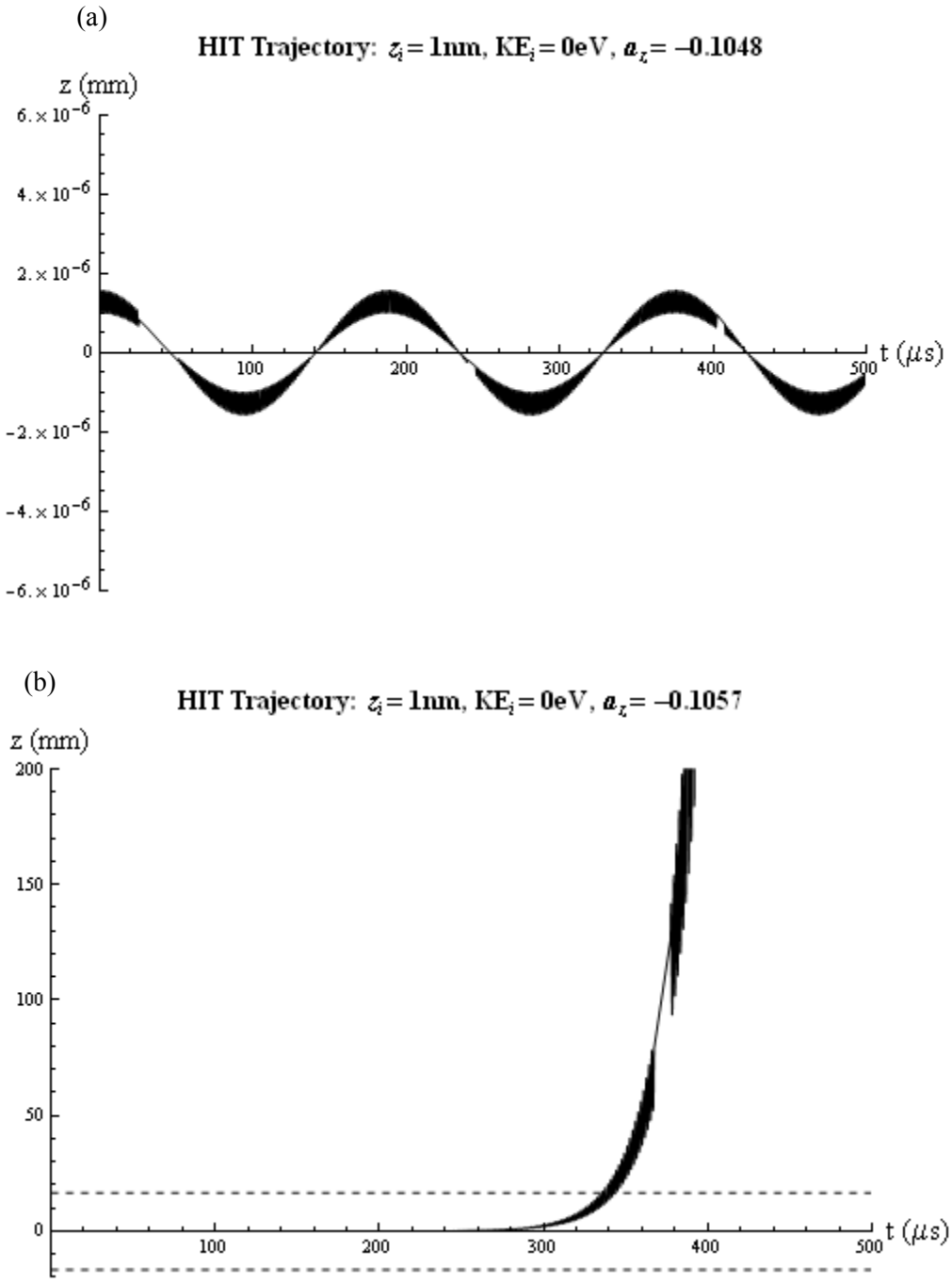

Figure 5: HIT ion trajectories for (a) $a_z = -0.1048$ (b) $a_z = -0.1057$. The dashed lines in (b) represent the physical dimensions of the ion trap: $r_0 = z_0 = 1.67$cm.

The result of the numerical mapping is shown in Figure 6. All of the a_z values for the numerically determined boundary are within 5×10^{-4} of the HIT theoretical boundary. One can conclude that the stability of ion trajectories in a HIT can be accurately determined through this numerical method.

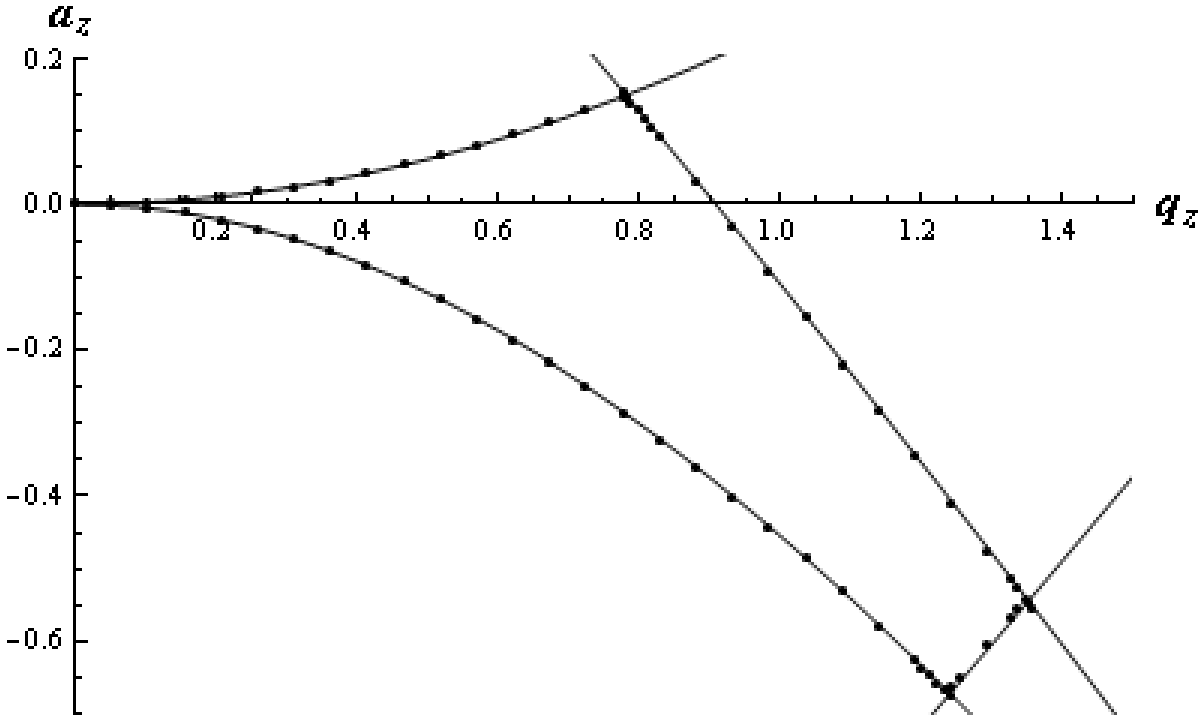

Figure 6: Numerically determined HIT stability region. The points in black show the numerically determined boundaries of the stable region. The black curves represent the theoretical stability boundaries.

Numerical Calculation of the CIT Stable Region

With the numerically determined stability diagram for a HIT found to be effectively identical to the theoretical stability diagram, and since the equations of motion for ions confined by a CIT are very close to the Mathieu equation, the same numerical method will provide the best approximation for the CIT ion trajectories. Using the same procedure outlined in the previous section, where Eq. 2.17 and 2.18 are used instead of Eq. 2.1 in step 3, example CIT ion trajectories are shown in Figure 7 using the same q_z value as the trajectories in Figure 5.

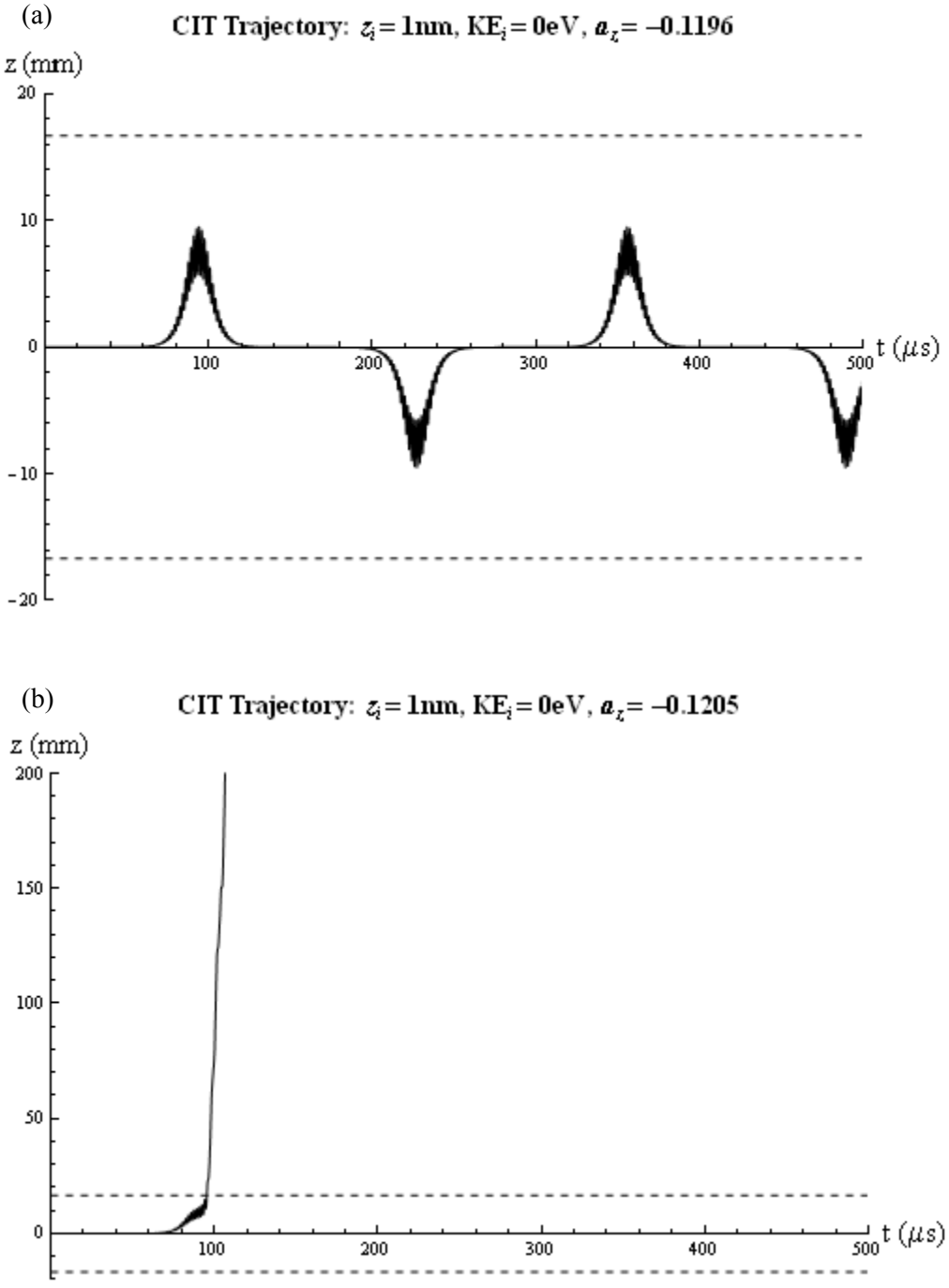

Figure 7: CIT ion trajectories for (a) $a_z = -0.1196$ (b) $a_z = -0.1205$. The dashed lines in the two plots show the physical dimensions of the ion trap: $r_0 = z_0 = 1.67$cm.

Unlike the trajectory in Figure 5a, the stable ion trajectory in Figure 7a has a greater displacement from the origin. This feature is undoubtedly due to the scaling of the Mathieu equation by the appearance of Eq. 2.15 and 2.16 in Eq. 2.17 and 2.18 respectively. Figure 7b depicts an unstable trajectory with an a_z value 0.0009 away from that used in Figure 7a and is lost within 100μs. Note that the same q_z value is used in the numerical calculation for the HIT trajectories in Figure 5. The CIT boundary point is located at $a_z = -0.1201 \pm 5x10^{-4}$ which is 0.0148 a_z units beyond the HIT boundary point for $\beta_z = 0$. This scheme is performed for 81 different values for q_z to map the boundaries of the stable region for a CIT. The result of this mapping is shown in Figure 8.

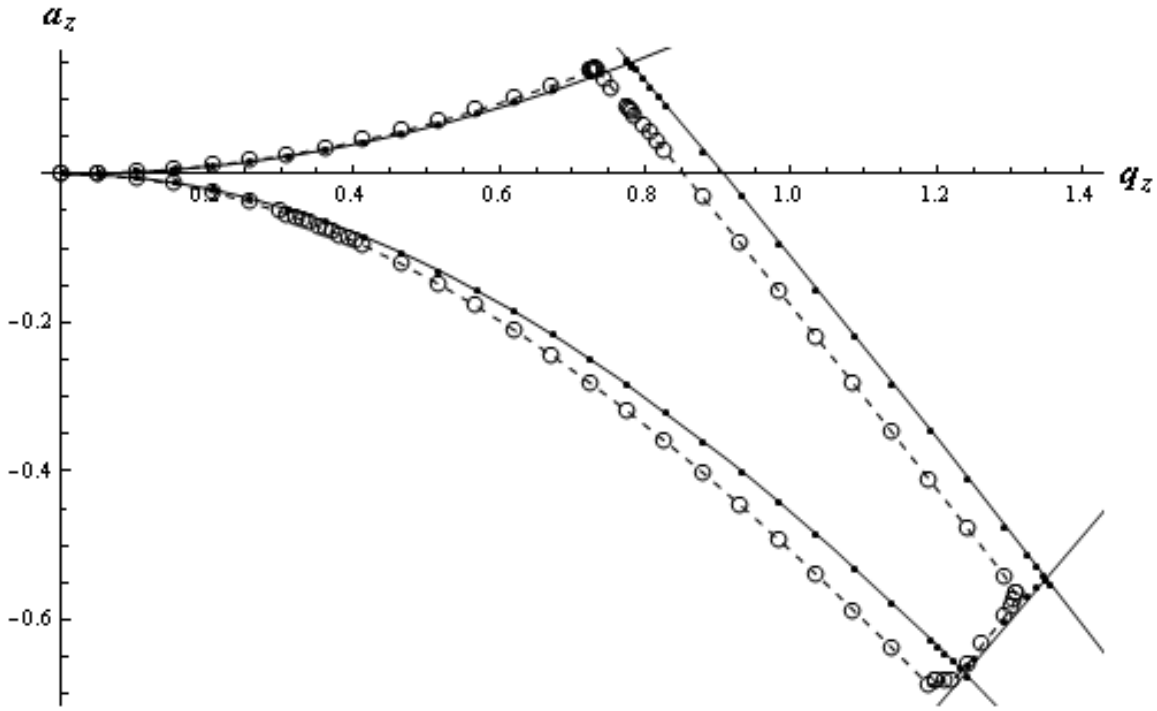

Figure 8: The numerically determined stability region for a CIT is shown by the open circles where the dashed line connects these points. The numerically calculated HIT stability region is represented by the filled circles. The theoretical HIT stability region is represented by the black curves.

Influence of Ion Energy on Stability Region

As mentioned previously, the initial conditions play no role in the stability of an ion when confined by a HIT. To illustrate this feature of the Mathieu equation, the same Mathieu parameters used for the trajectories depicted in Figure 5 are recalculated with an initial axial kinetic energy of 0.1eV and are shown in Figure 9. Even though the ion trajectory exceeds the physical dimensions of the trap in Figure 9a, the ion's trajectory is still stable where the ion periodically returns to the center of the trap. The stability of the ion is consistent with the ion trajectory for initial ion energy of zero as seen in Figure 5a. Figure 9b shows that the ion has an unstable trajectory but is lost much sooner than the ion in Figure 5b due to the difference in initial ion energy. It should be noted that the potential surfaces of the HIT in the theoretical treatment extend out to infinity and are non-zero while the HIT is completely transparent to the ions. This is why ion trajectories are always stable for Mathieu parameters located inside the stable region, regardless of the initial ion energy. To illustrate this feature, consider the trajectory in Figure 9c where the initial ion energy is set to 100eV.

The independence of ion energy for the HIT stability region may not apply to the CIT. As mentioned previously, the functions $\eta(r, z)$ and $\chi(r, z)$ vary dependent upon the location of the ion inside the CIT. To determine if these functions change the shape of the stability boundary assuming a non-zero initial kinetic energy, the aforementioned numerical method is used where now the initial ion velocity is non-zero.

To see how a non-zero initial energy may influence the CIT ion trajectories, example trajectories with an initial axial kinetic energy of 0.1eV at $q_z = 0.4636$ are shown in Figure 10. In Figure 10b, the ion is seen to have an unstable trajectory when $a_z = -0.1178$ with this initial axial kinetic energy of 0.1eV whereas Figure 7a depicts a stable trajectory for $a_z = -0.1196$ when the initial kinetic energy is set to zero. The influence of this non-zero initial energy causes the boundary to shift, where for this value of q_z, the 0.1eV boundary is located 0.0018 in a_z units above the zero energy boundary. By comparing Eq. 2.1 for the HIT and Eq. 2.17-18 for a CIT, the

(a)

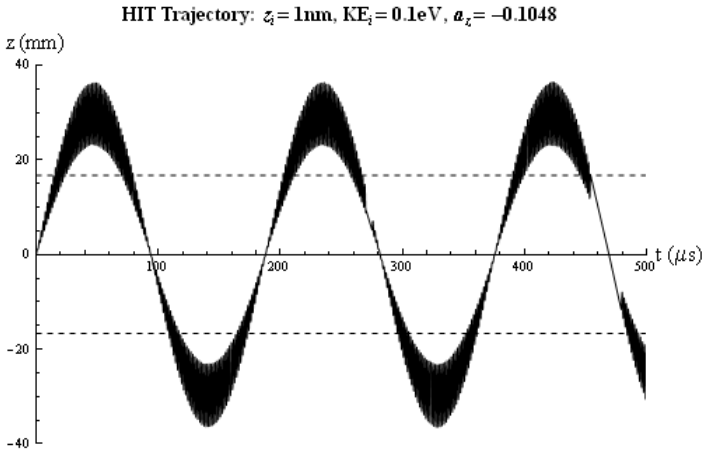

(b)

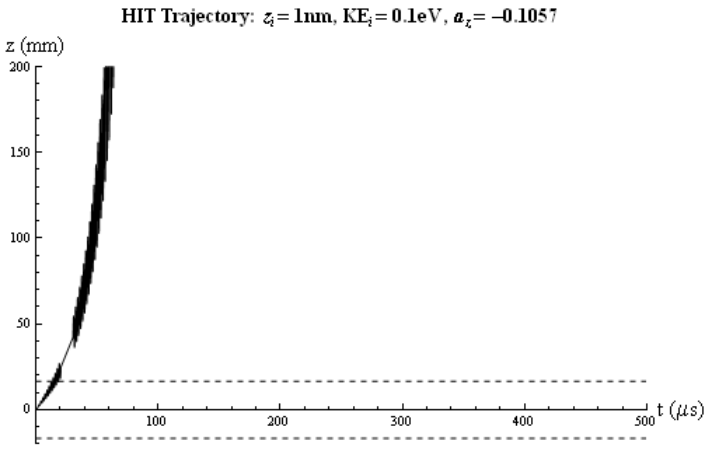

(c)

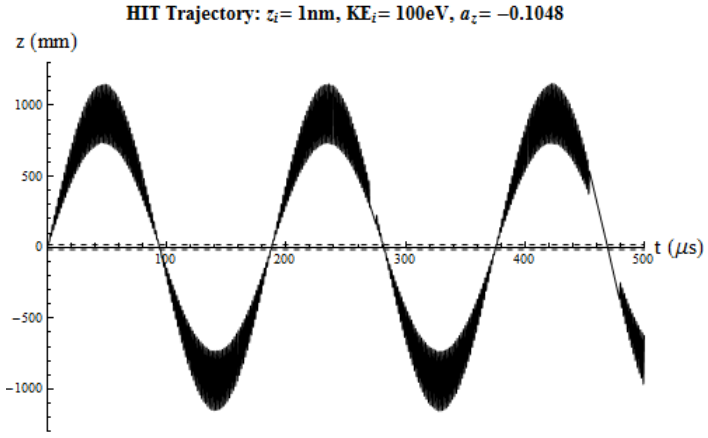

Figure 9: HIT trajectories for KE_i= 0.1eV (a) $a_z = -0.1048$, (b) $a_z = -0.1057$, and (c) $a_z = -0.1048$ with KE_i= 100eV. The dashed lines in the plots show the physical dimensions of the ion trap: $r_0 = z_0 = 1.67$cm.

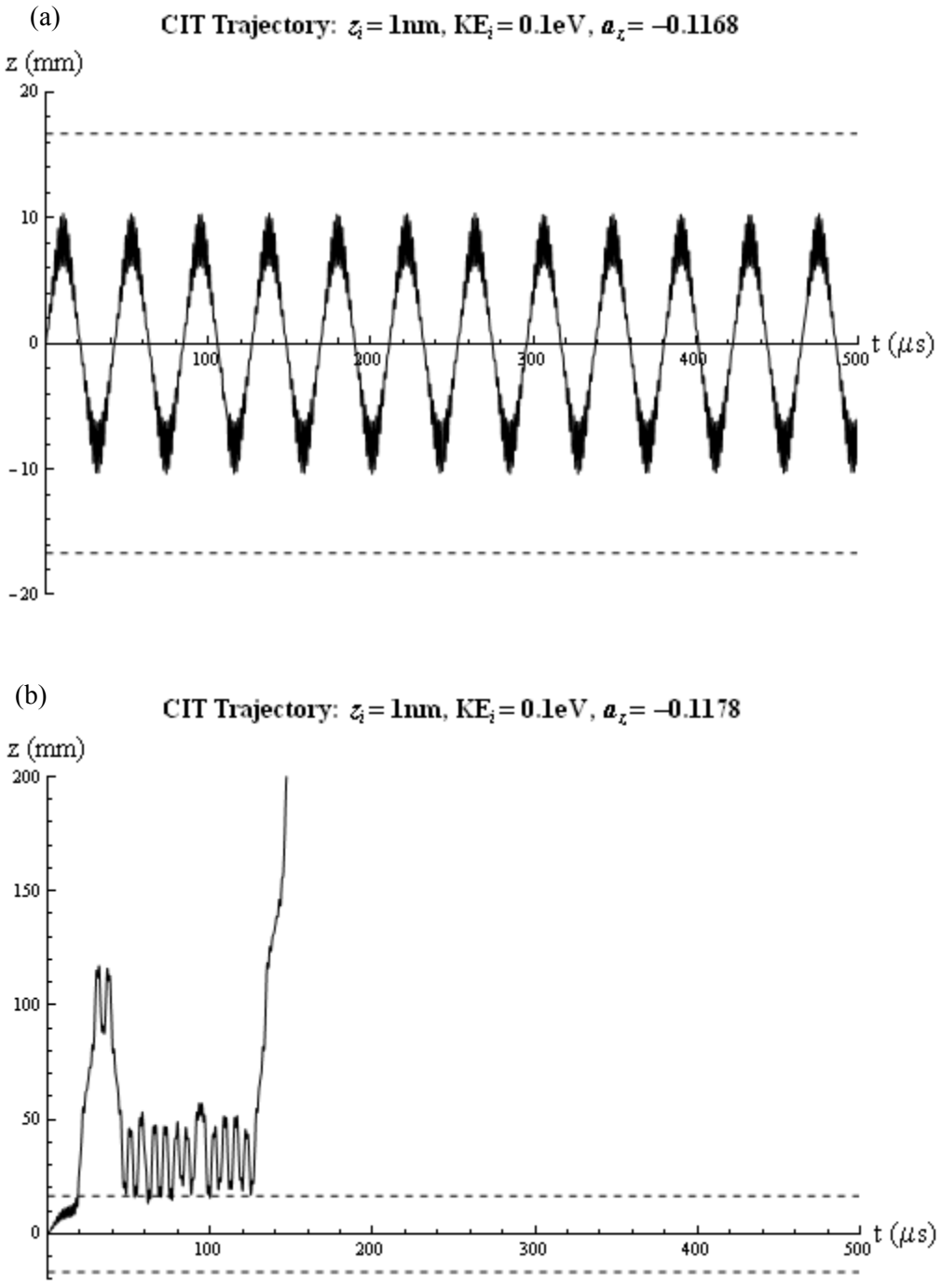

Figure 10: CIT ion trajectories with KE_i=0.1eV (a) $a_z = -0.1168$ and (b) $a_z = -0.1178$. The dashed lines in the two plots show the physical dimensions of the ion trap: $r_0 = z_0 = 1.67$cm.

energy dependence of the stability boundary seems to originate from the functions $\chi(r,z)$ and $\eta(r,z)$. The consequence of the position dependent functions $\chi(r,z)$ and $\eta(r,z)$ is an energy dependent stability region, where Mathieu parameters located beyond the boundary or exceeding the energy threshold will result in an unstable trajectory.

Figure 11 shows the $\beta_z = 0$ and $\beta_r = 0$ energy dependent boundaries for the initial ion kinetic energies of 0.01eV and 0.1eV. These boundaries were numerically determined for direct comparison with the experimental measurements. The energy dependent boundaries for $\beta_z = 1$ and $\beta_r = 1$ are not calculated. Since the energy dependence of the stability boundaries can be used to estimate the mean energy of the trapped ion in the experiment, a comparison of these energy dependent boundaries to the experimentally determined boundaries will be discussed in Chapter 5. Along with ion energy, the initial ion position will also influence the stability of the ion trajectories. Since an energy range for the confined ions can be estimated for the experiment discussed in Chapter 4, the ion's mean energy can be estimated by matching the experimental boundaries with the numerically calculated boundaries. The position dependence of the stability boundaries is outside the scope of this investigation and warrants further study.

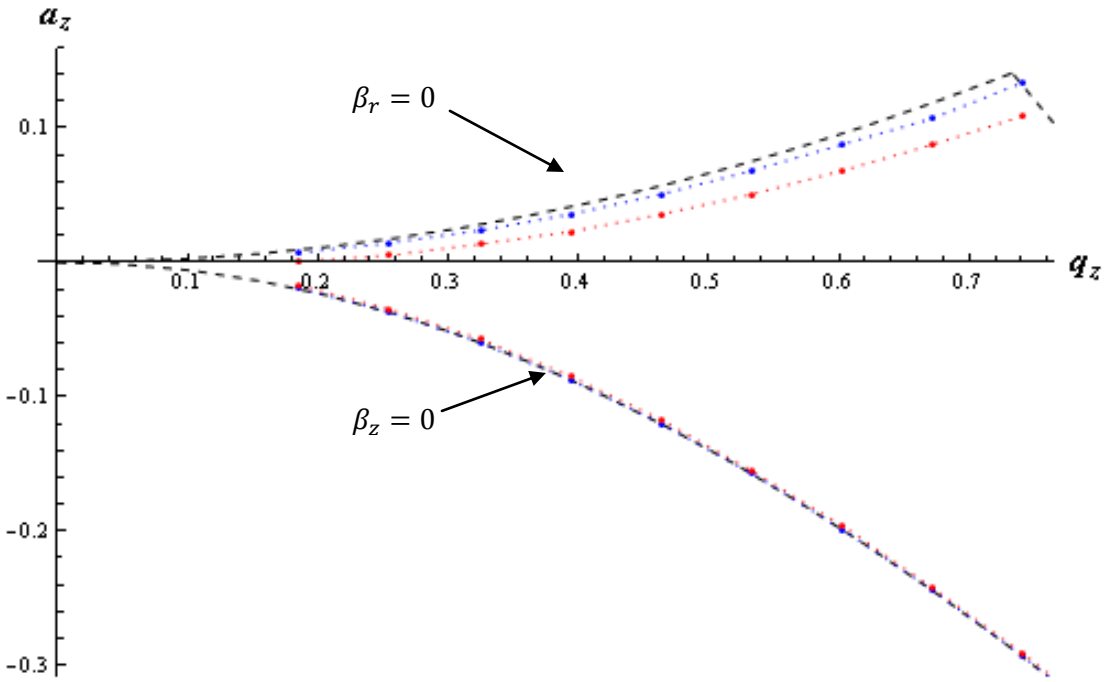

Figure 11: The zero energy CIT stability region is shown in black. The blue and red points represent the 0.01eV and 0.1eV energy dependent boundaries respectively. The colored dashed lines connect the numerically determined boundary points. The 0.01eV and 0.1eV energy dependent boundaries for $\beta_z = 0$ are difficult to discern due to the closeness of the boundaries.

CHAPTER 4

EXPERIMENTAL APPARATUS, PROCEDURE, AND METHODS

This chapter will provide an overview of the apparatus used to experimentally determine the boundary of the CIT. This includes discussions on the vacuum system as well as the components required for the creation, storage, and detection of ions. This chapter will also provide the methods and procedures used for the boundary mapping experiment.

The Experimental Apparatus

The facility used for this experiment is capable of attaining an ultra-high vacuum, where a background pressure of 4×10^{-11} Torr is achieved through the use of several components. A Varian Turbo V-550 turbomolecular pump is connected to a vacuum chamber, which houses the electron gun, CIT, time-of-flight (TOF) mass spectrometer, and multichannel (MCP) detector, and backed by a dual stage rotary vane pump (Varian SD-450 or Alcatel 2020A). A closed loop cooled water supply is connected to the turbomolecular pump to help dissipate the frictional heat buildup generated by the bearings. Several safety features are incorporated into the facility to ensure vacuum is maintained in the event of component failure. One such safety feature is the triggering of a pneumatic valve when the roughing pump foreline pressure exceeds the threshold of 100 milliTorr, preventing pump oil and other contaminants from reaching the vacuum chamber. Another safety feature is the water temperature and flow monitor. This device monitors the status of the closed loop cooled water supply system and will automatically switch to tap water if the temperature or pressure of the closed loop system is outside the acceptable range.

External to the vacuum chamber are two gas reservoirs, one filled with ultra high purity N_2 and one filled with He for this experiment. The two reservoirs are connected to a cold trap backed by a roughing pump. Prior to performing measurements, each reservoir is filled and evacuated several times while connected to the cold trap for the purpose of minimizing the

impurities in the reservoirs. Once the reservoirs are filled, the gas is introduced into the vacuum chamber through an adjustable leak valve, one for each reservoir. A residual gas analyzer, Masstorr DX100, is used to measure the pressure inside the vacuum chamber.

The main components encased in the vacuum chamber that control the creation, storage, ejection, and detection of ions are included in the schematics in Figure 12. A Spectra-Mat BaO electron gun is situated next to the CIT and produces ions via electron impact ionization (EII). The filament of the electron gun consists of tungsten and barium oxide and was selected due to higher emission current densities at lower operating temperatures [26]. The cathode is heated through the application of a 5.0 to 5.5V potential difference. A negative bias voltage of 105V is applied to the cathode to accelerate electrons into the CIT to generate ions. During ion storage, a positive bias voltage of 300V is applied to the cathode to inhibit the creation of additional ions during their confinement.

Ions are stored in a CIT with geometry $r_0 = z_0 = 1.67\text{cm}$. The electrodes of the CIT are constructed from 30 gauge 304 stainless steel mesh due to its non magnetic properties. Four symmetric 5mm diameter regions of the ring electrode have a smaller mesh density compared to other regions of the CIT to allow unobstructed laser light access to the center of the CIT, although lasers are not used in this experiment.

In order to eject the ion cloud from the CIT for subsequent acceleration into the TOF drift tube, the ring electrode of the CIT is grounded and high voltages of +226V and -246V are applied to the endcaps. A potential of -1400V applied to the TOF drift tube causes the ejected ions to separate spatially by their mass-to-charge ratios. A collimating lens, at a potential of -280V, is situated near the entrance of the drift tube. Its inclusion in the facility increases the collection efficiency of the TOF/detector system.

Ion detection is achieved through the use of a pair of high gain Burle 25mm microchannel plates (MCPs) in the chevron configuration and are situated at the end of the TOF drift tube. A large potential difference of -1800V is applied to the MCP for its linear operation.

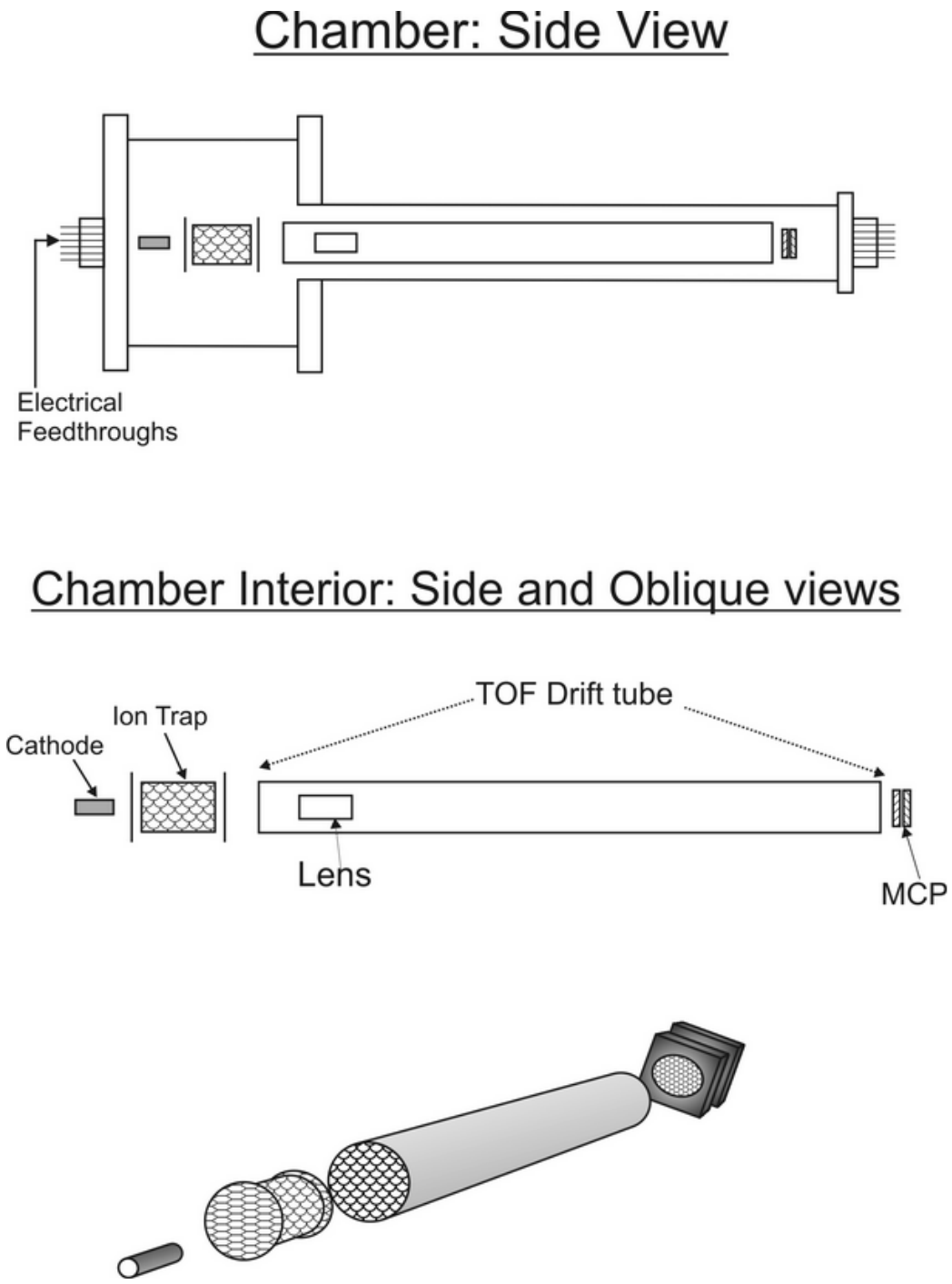

Figure 12: Schematics of the essential components needed for the creation, storage, ejection, and detection of ions. The electron gun cathode is used to generate ions through electron impact ionization. After ions are stored in the CIT for a user specified duration, ions are ejected from the CIT and are separated by their mass-to-charge ratios in the TOF drift tube. Ions are then detected by the MCP detector.

The amplified ion signal is then sent to a Tektronix 680C oscilloscope where the resulting TOF spectrum is digitized and saved on a Gateway E-4200 computer.

Experimental Procedure

The procedure used to experimentally determine the stable region of the CIT incorporates various aspects of the creation, storage, and detection of ions. With reference to Figure 13, ion creation is initiated by the timing control system switching the positive bias on the cathode to negative. Electrons then enter the CIT and ionize the confined gas through EII. During this time, a biased ac potential used to confine the ion of interest is applied to the ring electrode where the endcaps are held at ground. The applied CIT potentials are measured through coupling a Tektronix 680B oscilloscope probe to the trap's electrical feed through from the vacuum chamber. The oscilloscope provides an accurate measurement of the applied potential, where the amplitude is measured within 2.5% and the DC offset can be measured to within 0.1V. The negative bias on the cathode is applied for 5ms before it is again switched positive to inhibit further ion creation.

The N_2 gas introduced into the vacuum chamber provides the source for the ion used in this study, N^+ with mass-to-charge ratio 14 amu/e. Since the largest contaminant inside the vacuum chamber is water, this ion is selected because it does not charge transfer with water. He is also introduced into the chamber and is used to collisonally cool the ions. This cooling reduces the average kinetic energy of the ions where the size of the ion cloud is estimated to have a radius of 1mm. The pressures used in the experiment are $P_{N_2} = 1.16\text{x}10^{-8}$ Torr $\pm$ 6% and $P_{He} = 2.6\text{x}10^{-6}$ Torr $\pm$ 8% where the reported error represents the error in the ion gauge pressure calibration. These pressures for N_2 and He are selected since experimental measurements have shown that the FWHM of the ion signals for N^+ is constant for storage times greater than 600ms. Since the FWHM is related to the average size of the ion cloud before ejection, the constancy of the FWHM indicates that the size of the ion cloud is not changing. As a result, the N^+ ions are in

stable equilibrium with the buffer gas and the energy supplied to the ions through RF heating. A calculation of the collision period at these pressures, shown in Appendix III, is found to be 27 ms. Through using storage times of 690ms and 700ms for the durations of U_{01} in the experiment, as seen in Figure 13, N^+ undergoes approximately 25 collisions with the He atoms.

In the experiment, measurements are performed in a manner similar to the procedure used to numerically determine the stability regions in Chapter 3. An ion with a mass-to-charge ratio of 14 amu/e is selected along with a frequency of 600KHz. The boundary is found by scanning the value of a_z for a selected value of q_z. One difference between the numerical and experimental procedures is the use of two different values for a_z during ion storage in the experiment as seen in Figure 13 for dump 2. The DC offset U_{01}, which is proportional to a_z, is selected so as to maximize the number of ions confined in the trap. An ion intensity mapping of the stability region in Appendix IV shows the location of maximized ion number density. The signal intensity measurement at dump 1, which has a duration of 690ms, is performed to ensure that the initial ion population is nonzero.

The second dump pulse seen in Figure 13 has a duration of 701.5ms and has two different DC offsets applied during ion confinement. As before, U_{01} is initially applied but now for a duration of 700ms. The DC offset is then abruptly switched to U_{02} and is used to search for the boundary of the stability region. Calculations performed on the trajectories of ions confined by a CIT have shown that there is no change to the boundary by abruptly changing the DC offset in this manner. The calculations have also shown that all unstable ions escape the physical structure of the ion trap within 0.5ms. The duration of U_{02} is set to 1.5ms to ensure all unstable ions are expelled from the trap before ion ejection is initiated. This small duration of U_{02} is an order of magnitude smaller than the collision period, 27ms with the He buffer gas.

Once ion ejection is initiated, the RF potential applied to the ring electrode of the CIT is terminated on its rising edge as depicted in Figure 13. Measurements have shown that the ion signal resolution is optimized at this termination phase of the RF. This is caused by a “squeezing”

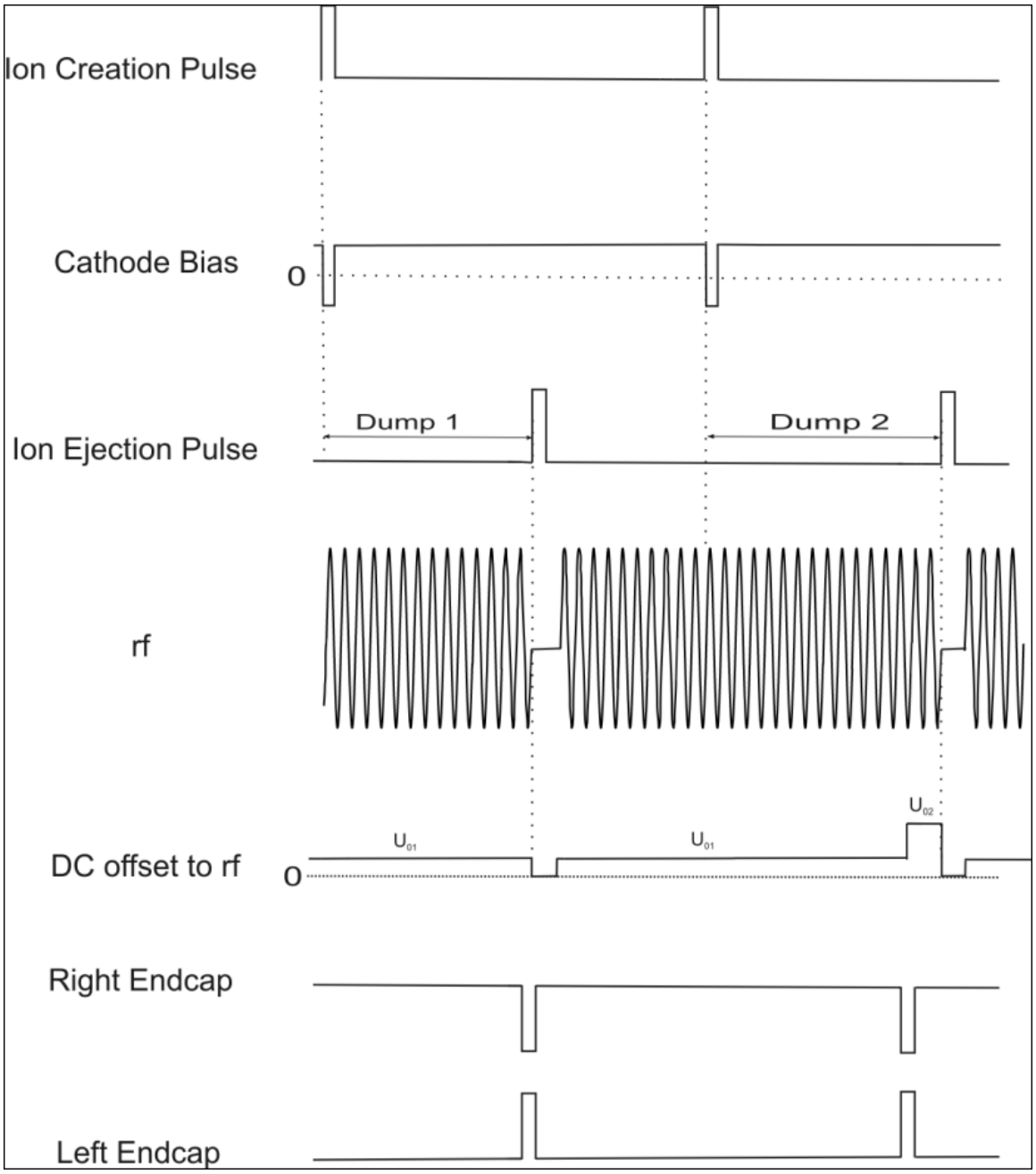

Figure 13: Timing diagram for the relevant components used in the experiment. The ion creation pulse triggers the positive bias on the cathode while the RF and U_0 is applied to the ring electrode of the CIT. Dump 1 has a duration of 690ms where the ion ejection pulse triggers the grounding of the RF on its rising edge while the endcaps receive high voltages for ion ejection. During dump 2, U_{02} is applied at 700ms of the confinement period and lasts for 1.5ms before ion ejection.

of the ion cloud in the z direction. This slight reduction of the axial spatial distribution just before ion extraction leads to the reduced signal width of the ion in the TOF distribution. Further information regarding the RF phase dependence of the ion spatial distribution in an ion trap can be found elsewhere [23,27].

Measurement Methods

Using a fixed frequency of 600KHZ, the Mathieu parameters for N^+ are adjusted by varying the amplitude and DC offset of the potential applied to the CIT. Following the timing diagram in Figure 13, the N^+ signal intensity is recorded 100 times for each dump delay to produce an averaged TOF distribution. As mentioned previously, U_{01} is selected so as to maximize the ion number density in the trap for the measurements at dump 1 and 2. The TOF distribution in Figure 14 is an example of a measurement for N^+ at dump 1 with Mathieu parameters q_z= 0.4636 and a_z= -0.0566.

In Figure 14, there is a noticeable presence of other ions in the TOF distribution. This is due to the background gas in the vacuum chamber and apart from the N^+ signal, is responsible for the presence of C^+, CH_3^+, O^+, OH^+, H_2O^+, and HDO^+ in the distribution. The Mathieu parameters for these ions place them inside the numerically calculated stable region for a CIT as shown in Figure 15.

With this maximized population for a fixed value for q_z for N^+, the a_z Mathieu parameter is changed after 700ms to access a different region of the stability diagram. This is done by simply changing the DC offset applied to the ring electrode of the ion trap, i.e. dump 2 in Figure 13. The experimental boundary is determined from the measurements of the signal intensity for N^+ at these alternate locations in the stability diagram. An example of such a measurement is included in Figure 16.

The TOF distribution in Figure 16 shows no ion signal for ions with mass-to-charge ratios above 14 amu/e. This is consistent with the stability diagram in Figure 17 which shows that

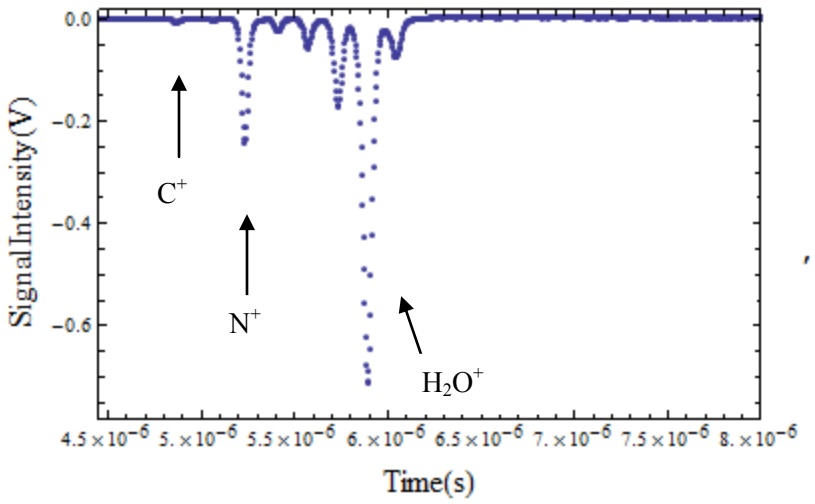

Figure 14: TOF distribution for N^+ Mathieu parameters q_z= 0.4636 and a_z= -0.0566. Other ions are noticeably present, ranging from m/q= 12 to 19 amu/e.

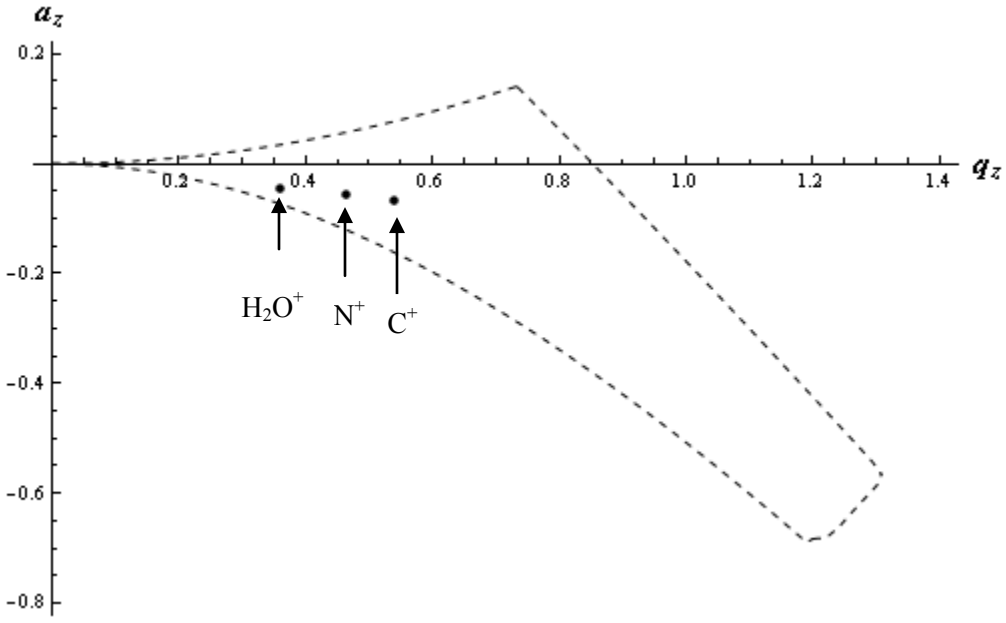

Figure 15: CIT stability diagram for N^+ Mathieu parameters q_z= 0.4636 and a_z= -0.0566. Other ions are shown in the diagram for comparison with Figure 14.

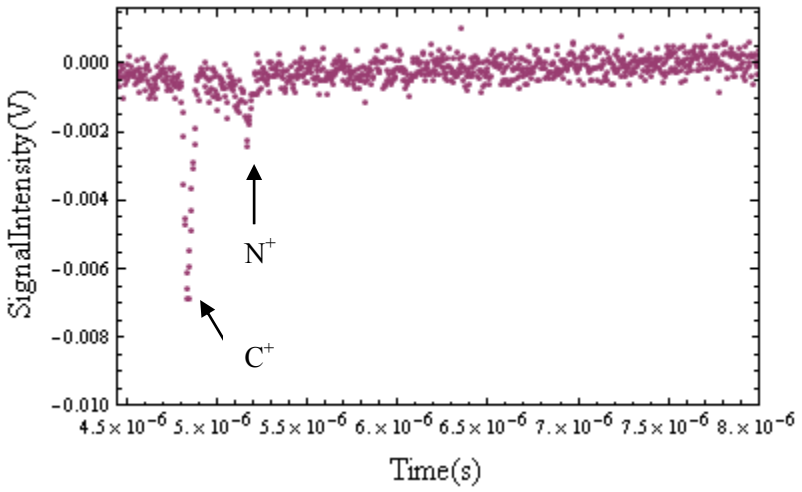

Figure 16: TOF distribution for N^+ Mathieu parameters q_z= 0.4636 and a_z= -0.1187.

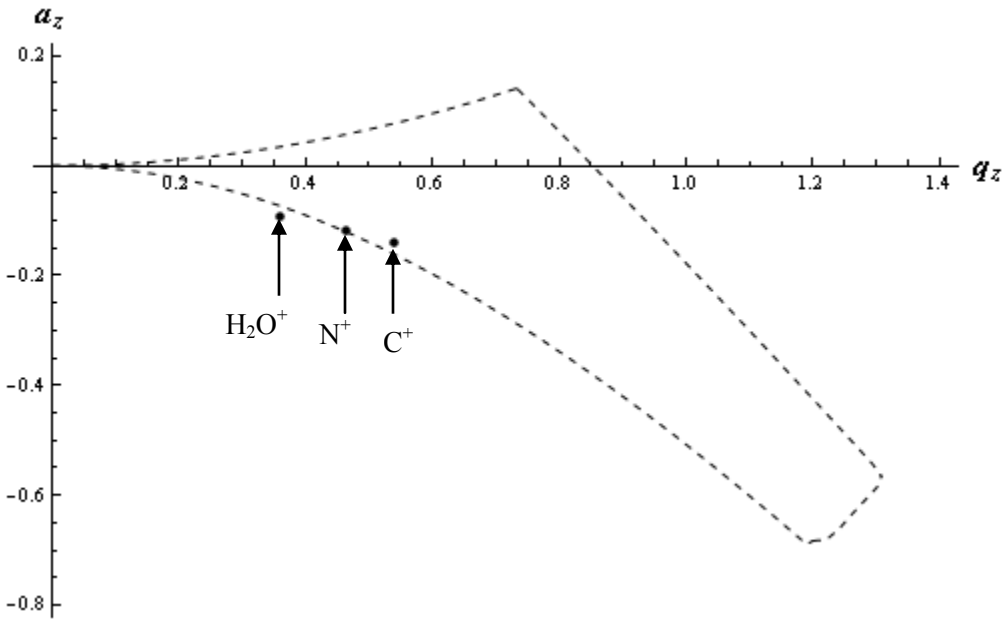

Figure 17: CIT stability diagram for N^+ Mathieu parameters q_z= 0.4636 and a_z= -0.1187. Other ions are shown in the diagram for comparison with Figure 16.

the Mathieu parameters for these ions place them outside the numerically calculated CIT stability region. Also note that the location for C^+ in the stability diagram suggests that these ions have stable trajectories where a signal for m/q=12 amu/e appears in the TOF distribution in Figure 16. As mentioned in Chapter 3, the initial energy of an ion can influence the stability/instability of its trajectory. This explains the reduction of the signal intensity of N^+ in Figure 16. As the Mathieu parameters for N^+ approach the boundary of the stable region, ions with kinetic energies above a certain threshold will lead to unstable trajectories. Ions with kinetic energies below this threshold have stable trajectories and remain trapped. Since Figure 16 indicates that some N^+ ions still have stable trajectories at a_z= -0.1187, another measurement must be performed in order to determine the location of the stability boundary. Through finding the a_z value that will lead to zero signal intensity for N^+, the experimental boundary is determined to be between the last a_z value that leads to a non-zero signal for N^+ and the a_z value that leads to no signal for N^+. An example of an a_z value leading to no signal for N^+ is shown in Figure 18.

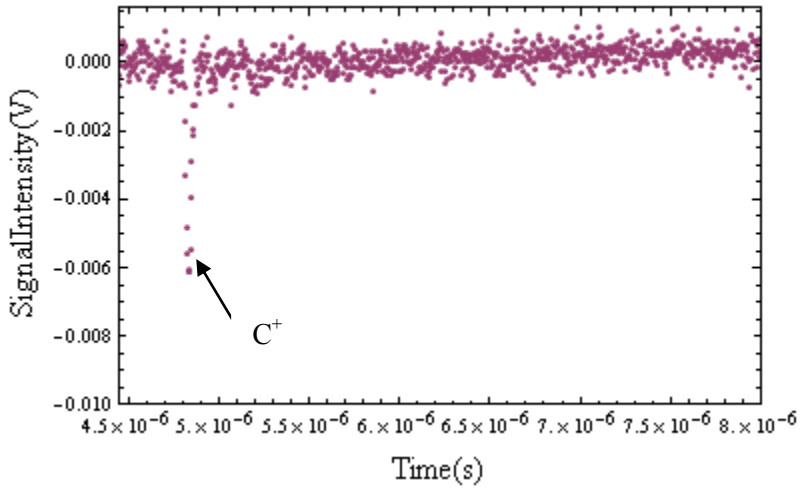

Figure 18: TOF distribution for N^+ Mathieu parameters q_z= 0.4636 and a_z= -0.1205.

As seen in Figure 18, no signal appears for N^+ in the distribution. This indicates that the location of the $\beta_z = 0$ boundary at q_z=0.4636 lies somewhere between a_z= -0.1187 and -0.1205.

A quantitative analysis of the signal area for N^+ in the TOF distributions is also used to determine the location of the boundary. A background subtracted peak area for the N^+ signal is calculated from each TOF distribution. In addition to this, the noise level is determined by calculating the peak area in a region of the TOF distribution where no signal appears. The difference between the signal peak area and the area associated to the noise is then computed, i.e. $\mathrm{Area}_{N^+} - \mathrm{Area}_{\mathrm{Noise}}$. When this value is strictly greater than 0, the a_z value is considered to lie inside the stable region. For example, the peak area in Figure 16 is 1.7 $x10^{-10}$ Vs with standard error 3 x 10^{-11} Vs. The noise level in Figure 16 is 3 x 10^{-11} Vs and has a standard error of 2 x 10^{-11} Vs Using these values, one finds that difference in areas is 1.4 x 10^{-10} Vs and has an error of 4 $x10^{-11}$ Vs using error propagation, indicating that some of the N^+ ions are still stable at a_z= -0.1187.

When the difference between the signal and noise areas is 0 within the error, the signal for N^+ at dump 2 is indistinguishable from the noise and the a_z value for such a measurement is considered to lie outside the stable region. For the a_z= -0.1205 measurement shown in Figure 18, the difference between the signal and noise areas is found to be $3x10^{-11} \pm 4x10^{-11}$. Since a value less than 0 is within the error for this measurement, and clearly there is no signal for N^+ as seen in Figure 18, this indicates that a_z= -0.1205 lies beyond the stability boundary. With this information, the a_z location of the $\beta_z = 0$ at q_z=0.4636 is set as a_z= -0.1196 $\pm$ 0.0009. The difference between the peak and noise is calculated for all measurements to determine the boundary of the CIT. The result of the boundary mapping experiment as well as comparisons to the numerically calculated energy dependent boundaries for the CIT is discussed in Chapter 5.

CHAPTER 5

DISCUSSION OF RESULTS AND CONCLUSIONS

The experimental boundary of the CIT stability region is determined from 18 different locations in the stability diagram, ranging from $0.1854 \leq q_z \leq 0.7418$. The method discussed in Chapter 4 is applied to the measurements where the result is shown in Figure 19.

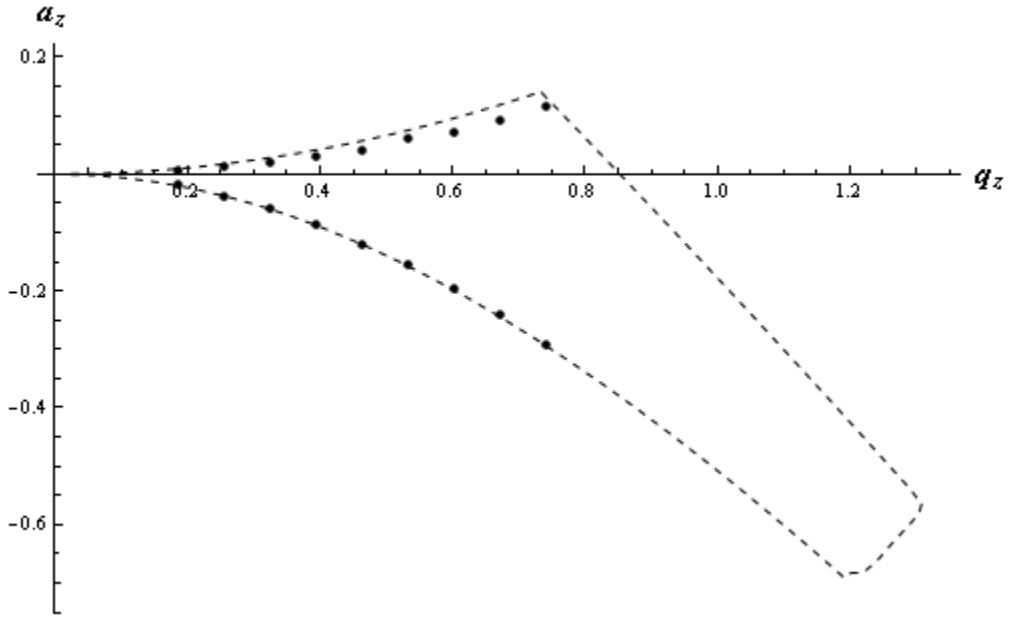

Figure 19: Stability diagram result for the boundary mapping experiment. The points in black represent the location of the experimentally determined boundary. The dashed lines again show the numerically determined stability region for a CIT assuming zero initial kinetic energy.

As seen in Figure 19, the measured points for the $\beta_z = 0$ and $\beta_r = 0$ boundaries are close to the numerically calculated boundaries. Since the average kinetic energy of N^+ is undoubtedly non zero in the experiment, the measured boundaries are expected to deviate from the zero energy CIT boundaries. The deviation of the experimental boundary from the numerically calculated energy dependent boundaries can be obtained by plotting the difference between the experimental and calculated boundary values for a_z, i.e. a_zEXP - a_zCalc. The error associated to a_zEXP - a_zCalc

and q_z are determined using error propagation (see Appendix V). A plot of a_zEXP - a_zCalc vs. q_z for the $\beta_z = 0$ boundary is shown in Figure 20. Note that the points in Figure 20 are in close proximity to each other, a consequence of the small change in the a_z boundary value for non-zero initial ion energies as seen in Figure 11. In order to understand this feature of the energy dependent boundaries for $\beta_z = 0$, a plot of Eq. 2.15 and 2.16 as a function of z is shown in Figure 21 where the radial displacement is set to zero.

As discussed in Chapter 2, the equations of motion for ion trajectories in a CIT have the form of the Mathieu equation but are scaled by the functions η and χ. Recall that ion stability is independent of the ion's initial kinetic energy for the HIT, yet stability is dependent on ion energy for the CIT trajectories. Therefore, the behavior of η influences the location of the energy dependent boundaries. Also note that for the $\beta_z = 0$ numerical calculations discussed in Chapter 3, the initial radial velocity is always set to zero and the radial displacement from the trap's center is set to a 1nm. As a consequence, the close proximity of the energy dependent boundaries for $\beta_z = 0$ may be attributed to the variation of η for $0 \leq z \leq z_0$ as seen in Figure 21.

Unlike the $\beta_z = 0$ boundary, the difference between the $\beta_r = 0$ energy dependent boundaries is quite large as seen in Figure 22. A plot of Eq. 2.15 and 2.16 as a function of r is shown in Figure 23 where the axial displacement is set to zero. The behavior of χ for $0 \leq r \leq r_0$ may be responsible for the large variation in the $\beta_r = 0$ boundaries. One interesting feature of Figure 20 and Figure 22 is that the experimentally determined boundaries are seen to lie between the 0.01eV and 0.1eV energy dependent boundaries. This is consistent with the N^+ ions attaining thermal velocities via collisional cooling with the He buffer gas.

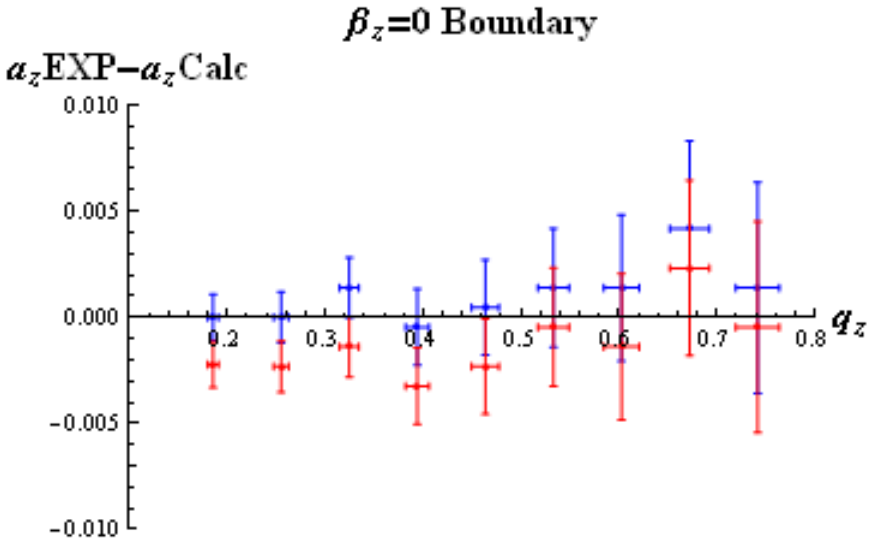

Figure 20: Plot of a_zEXP - a_zCalc vs. q_z for the $\beta_z = 0$ boundary. The points in blue and red are calculated using the 0.01eV and 0.1eV boundaries respectively.

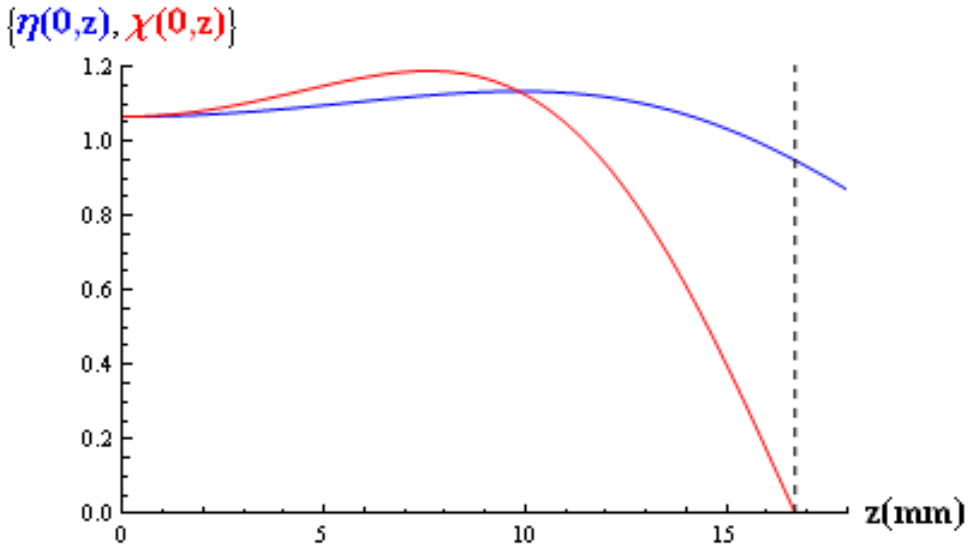

Figure 21: Plot of $\eta(0, z)$ and $\chi(0, z)$

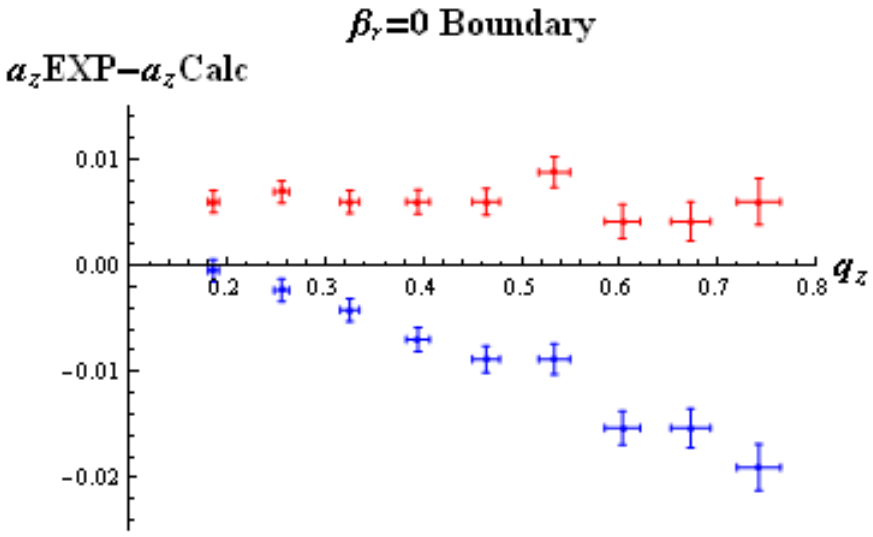

Figure 22: Plot of a_zEXP - a_zCalc vs. q_z for the $\beta_r = 0$ boundary. The points in blue and red are calculated using the 0.01eV and 0.1eV boundaries respectively.

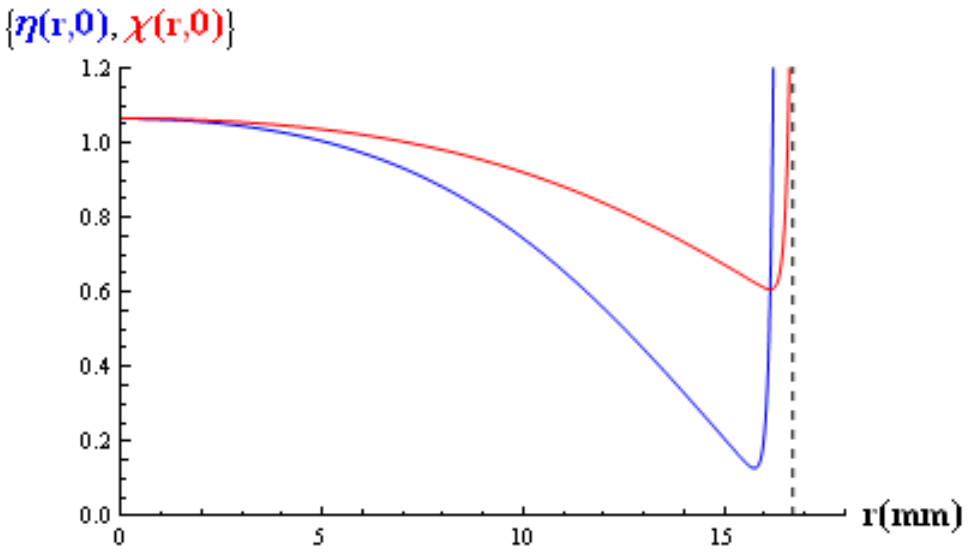

Figure 23: Plot of $\eta(r, 0)$ and $\chi(r, 0)$

Unfortunately, the boundaries for $\beta_z = 1$ and $\beta_r = 1$, as well as the remaining part of the $\beta_z = 0$ boundary cannot be experimentally determined from the measurements. This is due to a low signal to noise ratio for large values of q_z. The problem regarding low number density can potentially be solved for future measurements through using a combination of frequency, amplitude, and DC offset shifting during ion the storage phase to initially place the ion at the location of maximum ion number density in the stability region. However, such a scheme would have to be numerically investigated to determine how it would influence the stable region.

In summation, the CIT's experimentally determined stability boundaries for $\beta_z = 0$ and $\beta_r = 0$ are found to lie in close proximity to the numerically calculated zero energy boundaries. Since ion stability is dependent on ion energy for a CIT, discrepancies between two boundaries are expected due to the non-zero energy of the ions in the experiment. Energy dependent boundaries have also been calculated where all of the experimental boundary points are found to lie consistently between the 0.01eV and 0.1eV energy boundaries. This is consistent with the ion attaining thermal energies through collisional cooling with the He buffer gas. As a result, the numerically calculated $\beta_z = 0$ and $\beta_r = 0$ boundaries provides an adequate estimate of the shape of the stability region for use in selective ion stability. Furthermore, one may use the energy dependence of the CIT's stability region to estimate the mean energy of the trapped ions.

APPENDIX I

APPROXIMATING ION TRAJECTORIES FOR A CIT

Note that Eq. 2.17 and 18 are close to the form of the 2nd order Mathieu differential equation where the difference lies with the inclusion of the functions η and χ in the equations. The appearance of these terms couples the motion of the ion due to the dependence of both z and r in each function. As a consequence of this coupling, no analytic solution to these types of equations exists; however, we can make certain approximations regarding an ion's trajectory inside the CIT to simplify the equations. Suppose that an ion is confined in the CIT such that its trajectory stays relatively close to the origin. To determine how Eq. 2.17 and 18 behave as a result, the functions η and χ are shown in Figure 24 assuming the CIT has the geometry $r_0 = z_0 = 1.67\text{cm}$.

As seen in Figure 24, the values of the functions approach the same constant value for small displacements from the origin. For higher values of r and z, the functions begin to deviate from this value, yet for ion trajectories confined within 3mm from the trap's center, this value changes by no more than 2.8%. Therefore, for small displacements from the origin, $\eta(r,z) = \chi(r,z) = \text{constant}$ can be used in Eq. 2.17 and 18 to approximate the ion motion in the following way:

$$\frac{d^2u}{d\nu^2} + \left(a_u\eta - 2q_u\eta\cos(2\nu)\right)u = 0 \qquad (I.1)$$

The parameter u that appears in Eq. I.1 represents the motion in either the r or z direction. The parameter η represents the aforementioned constant and has a value of 2.06514. In a sense, Eq. 2.17 can be thought of as a scaling of the Mathieu equation by η. Since the Mathieu equation describes the motion of ions inside a HIT, we can clearly see that the motion of ions inside a CIT behave in a similar manner.

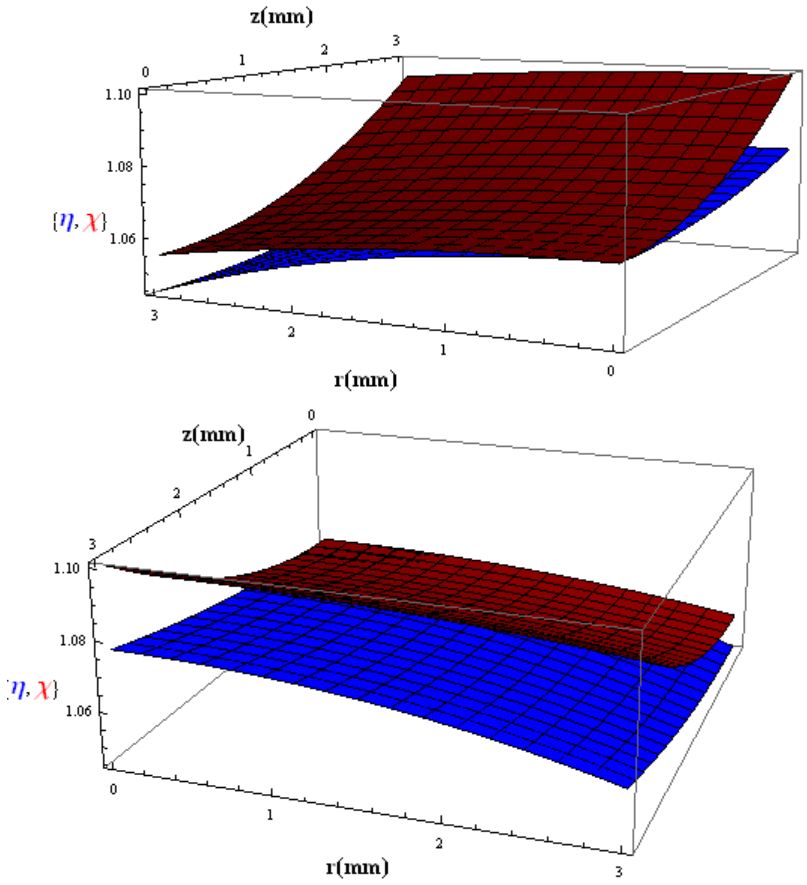

Figure 24: 3D plot of η and χ as functions of r and z. Since the functions are symmetric about the origin, only positive values from 0mm to 3mm for r and z are shown.

APPENDIX II

PSEUDOPOTENTIAL WELL APPROXIMATION

To gain further insight about the motion of the particles inside an ion trap, suppose we make some assumptions to simplify Eq. I.1. Let's suppose that the ion trajectory is composed of two parts: a macromotion $\bar{u}$ that slowly varies with respect to the applied RF, and a micromotion δ_u that responds with the RF. We then have the following:

$$u = \bar{u} + \delta_u, \qquad \bar{u} \gg \delta_u\ , \quad \frac{d\bar{u}}{dt} \ll \frac{d\delta_u}{dt} \tag{II. 1}$$

Using these relations in Eq. I.1, we find that the micromotion of the particle can be determined as follows:

$$\frac{du}{d\nu} = \frac{d\bar{u}}{d\nu} + \frac{d\delta_u}{d\nu} \cong \frac{d\delta_u}{d\nu}$$

$$\Rightarrow \frac{d^2\delta_u}{d\nu^2} = -\left(a_u\eta - 2q_u\eta\cos(2\nu)\right)(\bar{u} + \delta_u)$$

If $|a_u| \ll |q_u|$, and noting that the ion macromotion is assumed to be much greater than the micromotion amplitude, then

$$\Rightarrow \frac{d^2\delta_u}{d\nu^2} = 2q_u\eta\cos(2\nu)\bar{u}$$

Upon integrating this equation twice with respect to ν, the equation describing the ion's micromotion is

$$\delta_u = -\frac{q_u\eta}{2}\cos(2\nu)\bar{u} \tag{II. 2}$$

Therefore, we find that the ion's micromotion is linearly dependent upon the macromotion amplitude. Also, the ion micromotion is easily seen to be 180^0 out of phase with respect to the

applied RF. Using this result, the behavior of the ion macromotion can be determined by plugging this result back into Eq. I.1,

$$\frac{d^2u}{d\nu^2} = -\left(a_u\eta - 2q_u\eta\cos(2\nu)\right)(\bar{u} + \delta_u)$$

$$\Rightarrow \frac{d^2u}{d\nu^2} = -\left(a_u\eta - 2q_u\eta\cos(2\nu)\right)\left(1 - \frac{q_u\eta}{2}\cos(2\nu)\right)\bar{u}$$

$$\Rightarrow \frac{d^2u}{d\nu^2} = \left[-a_u\eta + 2q_u\eta\cos(2\nu) + \frac{a_u q_u\eta^2}{2}\cos(2\nu) - q_u^2\eta^2\cos^2(2\nu)\right]\bar{u}$$

Through integrating this result over one full cycle of the applied RF, the equation describing the macromotion of the ion can be found:

$$\frac{d^2\bar{u}}{d\nu^2} = \left\langle\frac{d^2u}{d\nu^2}\right\rangle = \frac{1}{\pi}\int_0^{\pi}\frac{d^2u}{d\nu^2}d\nu$$

$$\Rightarrow \frac{d^2\bar{u}}{d\nu^2} = -\left[a_u\eta + \frac{q_u^2\eta^2}{2}\right]\bar{u}$$

Upon converting this differential equation back into a function of time, we find that

$$\frac{d^2\bar{u}}{dt^2} = -\omega_u^2\bar{u} \qquad \text{(II. 3)}$$

i.e. a simple harmonic oscillator (SHO) with the macromotion frequency

$$\omega_u = \frac{\Omega}{2}\sqrt{a_u\eta + \frac{q_u^2\eta^2}{2}} \qquad \text{(II. 4)}$$

As a result, we see that the average motion of the particle can be treated as a SHO subjected to the following pseudopotential

$$V_{pseudo}(u) = \frac{1}{2e}m\omega_u^2u^2 \qquad \text{(II. 5)}$$

By equating $V_{pseudo}(r_0)$ to $V_{pseudo}(z_0)$, the Mathieu parameters that leads to the same pseudopotential well in all three degrees of freedom can be determined (4). This equation is called the spherical pseudopotential curve and has the following form :

$$a_z\text{spherical}(q_z) = -\frac{{q_z}^2\eta}{4}\left(\frac{4{z_0}^2 - {r_0}^2}{2{z_0}^2 + {r_0}^2}\right) \quad \text{(II. 6)}$$

This equation will prove to be very helpful in the experiment and is discussed further in Chapter 4.

Using Eq. II.1-4, the approximate solution to the ion's equations of motion is

$$u(t) = \left(A\cos(\omega_u t) + B\sin(\omega_u t)\right)\left[1 - \frac{q_u\eta}{2}\cos(\Omega t)\right] \quad \text{(II. 7)}$$

where the coefficients A and B are dependent upon the ion's initial position and velocity. Note that this derivation is only valid for ion motion that slowly varies with respect to the applied RF, i.e. $\omega_u \ll \Omega$. Therefore, there is an upper bound on the Mathieu parameter: $\eta q_z \leq 0.4$.

Previous work done with the Mathieu equation has shown that numerical solutions using the 4th order Runge Kutta integration method agrees with the analytic solutions to a high degree of accuracy. Since the equations of motion in a CIT are very close to the Mathieu equation, the Runge Kutta method can also be used to numerically solve Eq. 2.17 and 18. In order to determine how well Eq. II.7 approximates an ion's trajectory in a CIT, these numerical solutions are compared to Eq. II.7 in Figure 25.

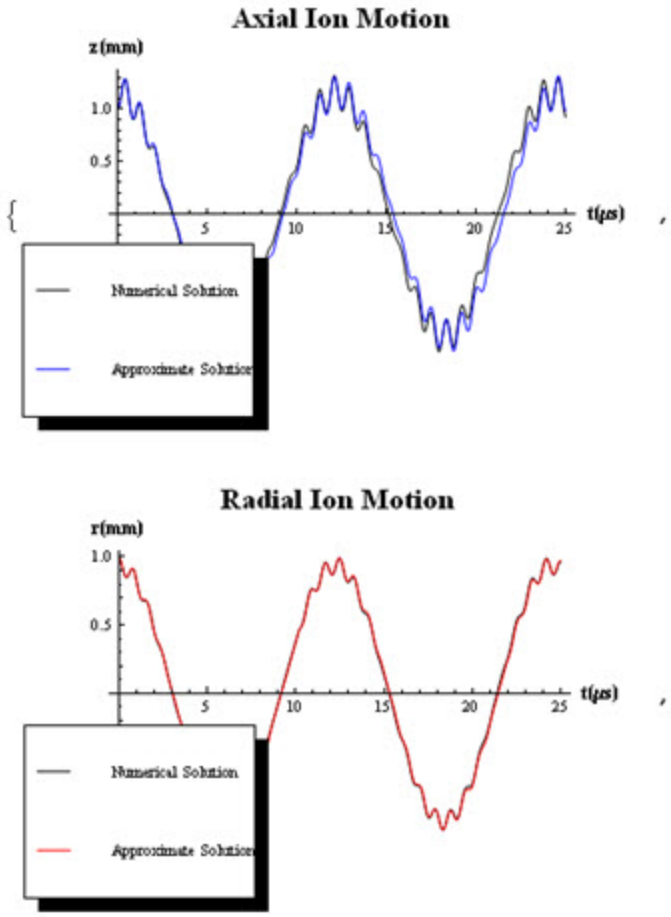

Figure 25: Numerical and approximate CIT ion trajectories. The values for q_z and a_z are 0.255 and -0.0174 respectively. The ion is assumed to have an initial displacement of 1mm from the trap's center in both the z and r directions with no initial velocity.

As seen in the above figure, the approximate solution (Eq. II.7) agrees very well with the numerical solution of the ion's trajectory in both the axial and radial directions. In summation, the motion of ions confined in a CIT can effectively be treated as a SHO responding to the pseudopotential defined in Eq. II.5, along with the superimposed micromotion given by Eq. II.2.

APPENDIX III

CALCULATION OF THE COLLISION PERIOD

In order to allow enough time for N^+ to cool via these collisions, the collision period between the buffer gas and ions must be determined. The collision period can be found through the following equation

$$\tau_{coll} = {}^{\lambda}/_{\bar{v}_{ion}} \qquad \text{(III. 1)}$$

where λ is the mean free path and $\bar{v}_{ion}$ is the average speed of the ion (28). The mean free path of the buffer gas can be calculated by the following equation

$$\lambda = \frac{kT}{\sqrt{2}\pi d^2 P} \qquad \text{(III. 2)}$$

where k is Boltzmann's constant, T is the temperature, d is the collision diameter, and P is the pressure of the buffer gas [28]. The buffer gas is in thermal equilibrium with the vacuum chamber walls, so T=298K. The diameter of the He and N^+ collision is taken to be the sum of the Van der Waals radii, or 2.9 angstroms. With a He pressure of 2.6×10^{-6} Torr, the mean free path is approximately 32 m. Assuming the ions have an average kinetic energy of 0.1 eV immediately after ion creation, the collision period is approximately 27ms.

APPENDIX IV

ION INTENSITY MAP OF THE STABLE REGION

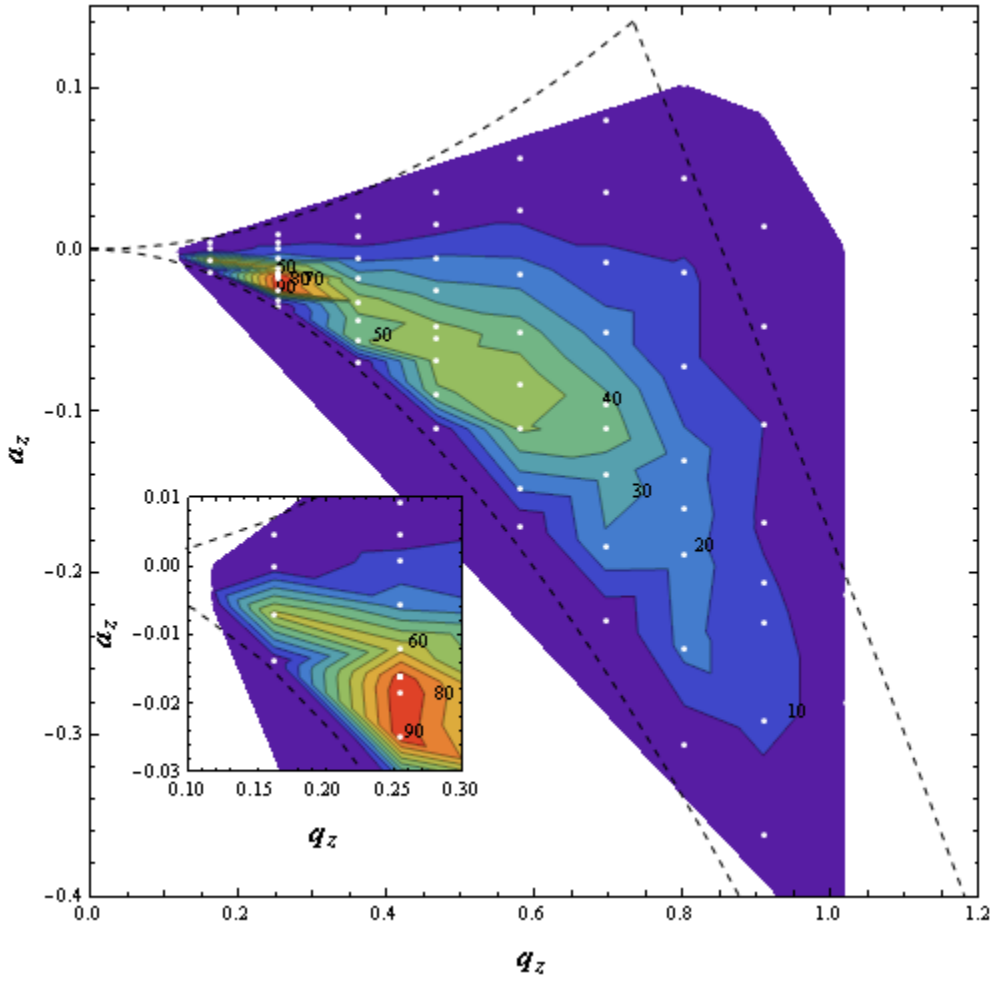

Figure 26: Intensity map of the stability diagram. The white points represent the Mathieu parameters used to generate the map. The colored regions represent the varying normalized signal intensity ranging from highest in red (100) to lowest in violet (0). The contours are determined through an interpolation of the intensities at the measurement points. The inset shows the ion intensity for small a_z and q_z.

APPENDIX V

ERROR PROPAGATION OF a_zEXP - a_zCalc AND q_z

The error associated to a_zEXP - a_zCalc and q_z are determined by the following equations

$$\sigma_{q_z} = \sqrt{\partial_{V_o}(q_z)^2 \, {\sigma_{V_0}}^2 + \partial_\nu(q_z)^2 \, {\sigma_\nu}^2} \tag{V.1}$$

$$\sigma_{a_{zExp-a_zCalc}} = \sqrt{\sigma_{a_z}EXP^2 + \sigma_{a_z}Calc^2 + \partial_\nu(a_z)^2 {\sigma_\nu}^2} \tag{V.2}$$

where terms of the form ∂_x denote a partial derivative with respect to x and σ_x represents the error of x. The error in the frequency of the applied RF potential, σ_ν, is 5KHz for the experiment. The error in amplitude, σ_{V_0}, is 2.5% of V_0. The errors for σ_{a_z}Calc and σ_{a_z}EXP are 0.0005 and 0.0009 respectively as mentioned in Chapter 3 and Chapter 4.

REFERENCES

1. Paul W., and H. Steinwedel. Z. Naturforsch A **8**, 448 (1953).
2. Berkling, K. Diplomarbeit. Physik. Inst. Univ. Bonn, Germany, (1956).
3. Fischer, E. A. Physik **156**, 26 (1959) .
4. Knight, R.. *Ph.D. Thesis.* Berkeley : University of California, Berkeley, 1979.
5. Benalin, B.M. and C. Audion. Int. J. Mass Spec. Ion Phys. **11**, 421 (1973).
6. Bonner, R.F., J.E. Fulford, R.E. March. Int. J. Mass Spectrom. Ion. Phys. **24**, 255 (1977).
7. Dehmelt, H.G. Adv. At. Mol. Phys. **3**, 53 (1967).
8. Dawson, P.H. and N.R. Whetton. J. Vac. Sci. Tech. **5**, 11 (1968).
9. Dawson, P.H. and C. Lambert. J. Vac. Sci. Tech. **12**, 941 (1968).
10. Dawson, P.H., J.W. Hedman, and N.R. Whetton. J. Sci. Instrum. **40**, 1444 (1969).
11. Dawson, P.H. and N.R. Whetton. Adv. Electron Phys. **27**, 59 (1969).
12. Dawson, P.H. and N.R. Whetton. Dyn. Mass Spec. **2**, 1 (1971).
13. Dawson, P.H. Int. J. Mass Spec. Ion. Phys. **14**, 317 (1974).
14. Dawson, P.H. and C. Lambert. Int. J. Mass Spec. Ion Phys. **14**, 339 (1974).
15. Dawson, P.H. and C. Lambert. Int. J. Mass Spec. Ion Phys. **16**, 269 (1975).
16. Dawson, P.H. *Quadrupole Mass Spectrometry and its Applications.* Amsterdam : Elsevier, 1976.
17. Dawson, P.H. and M. Meunier. Int. J. Mass Spec. Ion Phys. **29**, 269 (1979).
18. Todd, J.F.J. and R.M. Waldren. Int. J. Mass Spec. Ion Phys. **29**, 301 (1979).
19. Todd, J.F.J., R.M. Waldren, R.E. Mather, and G. Lawson. Int. J. Mass Spec. Ion Phys. **28**, 141 (1978).
20. Mather, R.E. G. Lawson, and J.F.J. Todd. Int. J. Mass Spec. Ion Phys. **28**, 347 (1978).
21. Waldren, R.M. and J.F.J. Todd. Int. J. Mass Spec. Ion Phys. **29**, 315 (1979).
22. Lawson, G., R.F. Bonner, and J.F.J. Todd. J. Phys. E: Sci. Ins. **6**, 357 (1973).
23. Van Fong, C.W. *Ph.D. Thesis.* Montreal : McGill University, 2001.

24. Abromowitz, M. and Stegun, I. *Handbook of Mathematical Functions with Formulas, Graphs, and Mathematical Tables.* New York : Dover, 1972.

25. Lee, W.W, C.H. Oh, P.S. Kim, M. Yang, and K. Song. In. J. Mass Spec. **230**, 25 (2003).

26. Jiang, Y. *Masters thesis. University of Nevada Las Vegas.* 1990.

27. Lichtenberg, Allan J. *Phase Space Dynamics of Prticles and Systems.* New York : John Wiley & Sons Inc., 1969.

28. Halliday, D., R. Resnik, and K.S. Krane. *Physics, Volume 1.* 5th Edition. New York : John Wiley & Sons Inc., 2001.

VITA

Graduate College
University of Nevada, Las Vegas

Bradley S. Clarke

Local Address:
1027 S. Rainbow Blvd. #148
Las Vegas, NV 89145

Degree:
Bachelor of Science, Physics, 2009
University of Nevada, Las Vegas, Las Vegas, NV

Bachelor of Science, Mathematics, 2009
University of Nevada, Las Vegas, Las Vegas, NV

Thesis Title: Numerical and Experimental Investigation of the Stability Region for a Cylindrical Ion Trap

Thesis Committee:
Chairperson, Dr. Victor Kwong
Committee Member, Dr. David Shelton
Committee Member, Dr. Stephen Lepp
Graduate Faculty Representative, Dr. Balakrishnan Naduvalath